

Planck intermediate results. XXII. Frequency dependence of thermal emission from Galactic dust in intensity and polarization

Planck Collaboration: P. A. R. Ade⁷⁵, M. I. R. Alves⁵¹, G. Aniano⁵¹, C. Armitage-Caplan⁷⁸, M. Arnaud⁶⁴, F. Atrio-Barandela¹⁷, J. Aumont⁵¹, C. Baccigalupi⁷⁴, A. J. Banday^{80,10}, R. B. Barreiro⁵⁸, E. Battaner^{82,83}, K. Benabed^{52,79}, A. Benoit-Lévy^{23,52,79}, J.-P. Bernard^{80,10}, M. Bersanelli^{31,44}, P. Bielewicz^{80,10,74}, J. J. Bock^{59,11}, J. R. Bond⁸, J. Borrill^{13,76}, F. R. Bouchet^{52,79}, F. Boulanger⁵¹, C. Burigana^{43,29}, J.-F. Cardoso^{65,1,52}, A. Catalano^{66,63}, A. Chamballu^{64,14,51}, H. C. Chiang^{25,6}, L. P. L. Colombo^{22,59}, C. Combet⁶⁶, F. Couchot⁶², A. Coulais⁶³, B. P. Crill^{59,72}, A. Curto^{5,58}, F. Cuttaia⁴³, L. Danese⁷⁴, R. D. Davies⁶⁰, R. J. Davis⁶⁰, P. de Bernardis³⁰, G. de Zotti^{40,74}, J. Delabrouille¹, F.-X. Désert⁴⁸, C. Dickinson⁶⁰, J. M. Diego⁵⁸, S. Donzelli⁴⁴, O. Doré^{59,11}, M. Douspis⁵¹, J. Dunkley⁷⁸, X. Dupac³⁷, T. A. Enßlin⁶⁹, H. K. Eriksen⁵⁵, E. Falgarone⁶³, F. Finelli^{43,45}, O. Forni^{80,10}, M. Frailis⁴², A. A. Fraisse²⁵, E. Franceschi⁴³, S. Galeotta⁴², K. Ganga¹, T. Ghosh⁵¹*, M. Giard^{80,10}, J. González-Nuevo^{58,74}, K. M. Górski^{59,84}, A. Gregorio^{32,42,47}, A. Gruppuso⁴³, V. Guillet⁵¹, F. K. Hansen⁵⁵, D. L. Harrison^{54,61}, G. Helou¹¹, C. Hernández-Monteagudo^{12,69}, S. R. Hildebrandt¹¹, E. Hivon^{52,79}, M. Hobson⁵, W. A. Holmes⁵⁹, A. Hornstrup¹⁵, A. H. Jaffe⁴⁹, T. R. Jaffe^{80,10}, W. C. Jones²⁵, E. Keihänen²⁴, R. Keskitalo¹³, T. S. Kisner⁶⁸, R. Kneissl^{36,7}, J. Knoche⁶⁹, M. Kunz^{16,51,2}, H. Kurki-Suonio^{24,39}, G. Lagache⁵¹, J.-M. Lamarre⁶³, A. Lasenby^{5,61}, C. R. Lawrence⁵⁹, J. P. Leahy⁶⁰, R. Leonardi³⁷, F. Levrier⁶³, M. Liguori²⁸, P. B. Lilje⁵⁵, M. Linden-Vørnle¹⁵, M. López-Caniego⁵⁸, P. M. Lubin²⁶, J. F. Macías-Pérez⁶⁶, B. Maffei⁶⁰, A. M. Magalhães⁵⁷, D. Maino^{31,44}, N. Mandolesi^{43,4,29}, M. Maris⁴², D. J. Marshall⁶⁴, P. G. Martin⁸, E. Martínez-González⁵⁸, S. Masi³⁰, S. Matarrese²⁸, P. Mazzotta³³, A. Melchiorri^{30,46}, L. Mendes³⁷, A. Mennella^{31,44}, M. Migliaccio^{54,61}, M.-A. Miville-Deschênes^{51,8}, A. Moneti⁵², L. Montier^{80,10}, G. Morgante⁴³, D. Mortlock⁴⁹, D. Munshi⁷⁵, J. A. Murphy⁷⁰, P. Naselsky^{71,34}, F. Nati³⁰, P. Natoli^{29,3,43}, C. B. Netterfield¹⁹, F. Noviello⁶⁰, D. Novikov⁴⁹, I. Novikov⁷¹, N. Oppermann⁸, C. A. Oxborrow¹⁵, L. Pagano^{30,46}, F. Pajot⁵¹, D. Paoletti^{43,45}, F. Pasian⁴², O. Perdereau⁶², L. Perotto⁶⁶, F. Perrotta⁷⁴, F. Piacentini³⁰, D. Pietrobon⁵⁹, S. Plaszczynski⁶², E. Pointecouteau^{80,10}, G. Polenta^{3,41}, L. Popa⁵³, G. W. Pratt⁶⁴, J. P. Rachen^{20,69}, W. T. Reach⁸¹, M. Reinecke⁶⁹, M. Remazeilles^{60,51,1}, C. Renault⁶⁶, S. Ricciardi⁴³, T. Riller⁶⁹, I. Ristorcelli^{80,10}, G. Rocha^{59,11}, C. Rosset¹, G. Roudier^{1,63,59}, J. A. Rubiño-Martín^{56,35}, B. Rusholme⁵⁰, E. Salerno⁹, M. Sandri⁴³, G. Savini⁷³, D. Scott²¹, L. D. Spencer⁷⁵, V. Stolyarov^{5,61,77}, R. Stompor¹, R. Sudiwala⁷⁵, D. Sutton^{54,61}, A.-S. Suur-Uski^{24,39}, J.-F. Sygnet⁵², J. A. Tauber³⁸, L. Terenzi⁴³, L. Toffolatti^{18,58}, M. Tomasi^{31,44}, M. Tristram⁶², M. Tucci^{16,62}, L. Valenziano⁴³, J. Valiviita^{24,39}, B. Van Tent⁶⁷, P. Vielva⁵⁸, F. Villa⁴³, B. D. Wandelt^{52,79,27}, A. Zacchei⁴², and A. Zonca²⁶

(Affiliations can be found after the references)

Preprint online version: April 24, 2022

ABSTRACT

Planck has mapped the intensity and polarization of the sky at microwave frequencies with unprecedented sensitivity. We use these data to characterize the frequency dependence of dust emission. We make use of the *Planck* 353 GHz *I*, *Q*, and *U* Stokes maps as dust templates, and cross-correlate them with the *Planck* and *WMAP* data at 12 frequencies from 23 to 353 GHz, over circular patches with 10° radius. The cross-correlation analysis is performed for both intensity and polarization data in a consistent manner. The results are corrected for the chance correlation between the templates and the anisotropies of the cosmic microwave background. We use a mask that focuses our analysis on the diffuse interstellar medium at intermediate Galactic latitudes. We determine the spectral indices of dust emission in intensity and polarization between 100 and 353 GHz, for each sky-patch. Both indices are found to be remarkably constant over the sky. The mean values, 1.63 ± 0.03 for polarization and 1.52 ± 0.02 for intensity, for a mean dust temperature of 18.7 K, are close, but significantly different. We determine the mean spectral energy distribution (SED) of the microwave emission, correlated with the 353 GHz dust templates, by averaging the results of the correlation over all sky-patches. We find that the mean SED increases for decreasing frequencies at $\nu < 60$ GHz, for both intensity and polarization. The rise of the polarization SED towards low frequencies may be accounted for by a synchrotron component correlated with dust, with no need for any polarization of the anomalous microwave emission. We use a spectral model to separate the synchrotron and dust polarization and to characterize the spectral dependence of the dust polarization fraction. The polarization fraction (*p*) of the dust emission decreases by $(34 \pm 10)\%$ from 353 to 70 GHz. We discuss this result within the context of existing dust models. The decrease of *p* could indicate differences in polarization efficiency among components of interstellar dust (e.g., carbon versus silicate grains), or, alternatively, it could be a signature of magnetic dipole emission from ferromagnetic inclusions within interstellar grains. Our observational results provide inputs to quantify and optimize the separation between Galactic and cosmological polarization.

Key words. Polarization – ISM: general – Galaxy: general – radiation mechanisms: general – radio continuum: ISM – submillimeter: ISM

* Corresponding author: tuhin.ghosh@ias.u-psud.fr

1. Introduction

*Planck*¹ (Tauber et al. 2010; Planck Collaboration I 2011) has mapped the polarization of the sky emission in seven channels at microwave frequencies from 30 to 353 GHz. The data open new opportunities to investigate the astrophysics of Galactic polarization. In this paper, we use these data to characterize the frequency dependence of dust polarization from the diffuse interstellar medium (ISM).

At microwave frequencies dust emission components include the long wavelength tail of thermal dust emission (Draine & Li 2007; Meny et al. 2007; Compiègne et al. 2011; Jones et al. 2013), the anomalous microwave emission (AME, Kogut et al. 1996; Leitch et al. 1997; de Oliveira-Costa et al. 1999; Banday et al. 2003; Lagache 2003; Davies et al. 2006; Dobler & Finkbeiner 2008; Miville-Deschênes et al. 2008; Ysard et al. 2010; Planck Collaboration XX 2011), and possibly dipolar magnetic emission of ferromagnetic particles (Draine & Lazarian 1999; Draine & Hensley 2013).

Thermal dust emission is known to be polarized, but to a different degree for each dust component, due to differences in the shape and alignment efficiency of grains (Hildebrand et al. 1999; Martin 2007; Draine & Fraisse 2009). The polarization of the $9.7\mu\text{m}$ absorption feature from silicates is direct evidence that silicate grains are aligned (Smith et al. 2000). The lack of polarization of the $3.4\mu\text{m}$ absorption feature from aliphatic hydrocarbons (along lines of sight towards the Galactic centre with strong polarization in the $9.7\mu\text{m}$ silicate absorption) indicates that dust comprises carbon grains that are much less efficient at producing interstellar polarization than silicates (Chiar et al. 2006). Observational signatures of these differences in polarization efficiency among components of interstellar dust are expected to be found in the polarization fraction (p) of the far infrared (FIR) and sub-mm dust emission. Spectral variations of polarization fraction have been reported from observations of star-forming molecular clouds (Hildebrand et al. 1999; Vaillancourt 2002; Vaillancourt et al. 2008; Vaillancourt & Matthews 2012). However, these data cannot be unambiguously interpreted as differences in the intrinsic polarization of dust components (Vaillancourt 2002); they can also be interpreted as correlated changes in grain temperature and alignment efficiency across the clouds. The sensitivity of *Planck* to low brightness extended emission allows us to carry out this investigation for the diffuse ISM, where the heating and alignment efficiency of grains are far more homogeneous than in star forming regions.

AME is widely interpreted as dipole radiation from small carbon dust particles. This interpretation, first proposed by Erickson (1957) and modelled by Draine & Lazarian (1998), has been developed into detailed models (Ali-Haïmoud et al. 2009; Silsbee et al. 2011; Hoang et al. 2011) that provide a good spectral fit to the data (Planck Collaboration XX 2011; Planck Collaboration Int. XV 2014). The intrinsic polarization of this emission must be small, due to the weakness or absence of polarization of the 220 nm bump in the UV extinction curve (Wolff et al. 1997), which is evidence of poor alignment of small carbon particles. The polarization fraction of the AME could be up to a few percent (Lazarian & Draine 2000; Hoang et al. 2013). The

Wilkinson Microwave Anisotropy Probe (WMAP, hereafter) data have been used to search for polarization in a few sources with bright AME, for example the ρ Ophiuchus and Perseus molecular clouds (Dickinson et al. 2011; López-Caraballo et al. 2011), yielding upper limits in the range of 1.5 % to a few percent on polarization fraction (Rubio-Martín et al. 2012).

Magnetic dipolar emission (MDE) from magnetic grains was first proposed by Draine & Lazarian (1999) as a possible interpretation of the AME. Draine & Hensley (2013) have recently revived this idea with a new model where the MDE could be a significant component of dust emission at frequencies from 50 to a few hundred GHz (Planck Collaboration Int. XIV 2014) and Planck Collaboration Int. XVII (2014), relevant to cosmic microwave background (CMB) studies. This hypothesis may be tested with the *Planck* polarization observations. The polarization fraction of MDE is expected to be high for magnetic grains. If the magnetic particles are inclusions within silicates, the polarization directions of the dipolar magnetic and electric emissions are orthogonal. In this case the models predict a significant decrease of the polarization fraction of dust emission at frequencies below 350 GHz.

WMAP provided the first all-sky survey of microwave polarization. Galactic polarization was detected on large angular scales at all frequencies from 23 to 94 GHz. The data have been shown to be consistent with a combination of synchrotron and dust contributions (Kogut et al. 2007; Page et al. 2007; Miville-Deschênes et al. 2008; Macellari et al. 2011), but they do not constrain the spectral dependence of dust polarization.

The spectral dependence of the dust emission at *Planck* frequencies has been determined in the Galactic plane and at high Galactic latitudes by Planck Collaboration Int. XIV (2014) and Planck Collaboration Int. XVII (2014). In this paper, we use the high signal-to-noise 353 GHz *Planck* Stokes I , Q , U maps as templates to characterize the spectral dependence of dust emission in both intensity and polarization. Our analysis also includes the separation of dust emission from CMB anisotropies. We extract the dust-correlated emission in intensity (I) and polarization (P) by cross-correlating the 353 GHz maps with both the *Planck* and WMAP data. For the intensity, we also use the $H\alpha$ and 408 MHz maps as templates of the free-free and synchrotron emission. The P and I spectra are compared and discussed in light of the present understanding and questions about microwave dust emission components introduced in Planck Collaboration Int. XVII (2014). We aim to characterize the spectral shape and the relative amplitude of Galactic emission components in polarization. In doing so we test theoretical predictions about the nature of the dust emission in intensity and polarization. We also provide information that is key to designing and optimising the separation of the polarized CMB signal from the polarized Galactic dust emission.

The paper is organised as follows. In Sect. 2, we introduce the data sets used in this paper. Our methodology for the data analysis is described in the following three sections. We define the part of the sky we analyse in Sect. 3. We describe how we apply the cross-correlation analysis (hereafter CC) to the intensity and polarization data in Sect. 4. Section 5 explains the separation of the dust and CMB emission after data correlation. The scientific results are presented in Sects. 6 and 7 for intensity, and Sects. 8 and 9 for polarization. The dust SEDs, I and P , are compared and discussed with relation to models of dust emission in Sect. 10. Section 11 summarizes the main results of our work. We detail the derivation of the correlation coefficients in Appendix A. Appendix B describes the Monte Carlo simulations we have performed to show that our data analysis is unbiased.

¹ *Planck* (<http://www.esa.int/Planck>) is a project of the European Space Agency (ESA) with instruments provided by two scientific consortia funded by ESA member states (in particular the lead countries France and Italy), with contributions from NASA (USA) and telescope reflectors provided by a collaboration between ESA and a scientific consortium led and funded by Denmark.

Appendix C describes the dependence of the dust I SED on the correction of the $H\alpha$ map, used as template of the free-free emission, for dust extinction and scattering. The power spectra of the maps used as templates of dust, free-free and synchrotron emission are presented in Appendix D for a set of Galactic masks.

2. Data sets used

Here we discuss the *Planck*, *WMAP*, and ancillary data used in the paper and listed in Table 1.

2.1. Planck data

2.1.1. Sky maps

Planck is the third generation space mission to characterize the anisotropies of the CMB. It observed the sky in seven frequency bands from 30 to 353 GHz for polarization, and in two additional bands at 545 and 857 GHz for intensity, with an angular resolution from $31'$ to $5'$ (Planck Collaboration I 2014). The in-flight performance of the two focal plane instruments, the HFI (High Frequency Instrument) and the LFI (Low Frequency Instrument), are given in Planck HFI Core Team (2011) and Mennella et al. (2011), respectively. The data processing and calibration of the HFI and LFI data used here are described in Planck Collaboration VIII (2014) and Planck Collaboration II (2014), respectively. The data processing specific to polarization is given in Planck Collaboration VI (2014) and Planck Collaboration III (2014).

For intensity, we use the first 15.5 months of the *Planck* mission (two full-sky surveys) with LFI and HFI data sets between 30 and 857 GHz. The LFI and HFI frequency maps are provided in HEALPix² format (Górski et al. 2005) with resolution parameters $N_{\text{side}} = 1024$ and 2048 , respectively. The *Planck* sky maps between 30 and 353 GHz are calibrated in CMB temperature units, K_{CMB} , so that the CMB anisotropies have a constant spectrum across frequencies. The two high frequency maps of *Planck*, 545 and 857 GHz, are expressed in MJy sr^{-1} , calibrated for a power-law spectrum with a spectral index of -1 , following the IRAS convention. We use *Planck* maps with the zodiacal light emission (ZLE) subtracted (Planck Collaboration XIV 2014) at frequencies $\nu \geq 353$ GHz, but maps *not* corrected for ZLE at lower frequencies because the extrapolation of the ZLE model is uncertain at microwave frequencies. Further it has not been estimated at frequencies smaller than 100 GHz. We do not correct for the zero offset, nor for the residual dipole identified by Planck Collaboration XI (2014) at HFI frequencies because it is not necessary for our analysis based on local correlations of data sets.

For polarization, we use the full *Planck* mission (five full-sky surveys for HFI and for LFI) data sets between 30 and 353 GHz. The *Planck* polarization that we use in this have been generated in exactly the same manner as the data publicly released in March 2013, described in Planck Collaboration I (2014) and associated papers. Note, however, that the publicly available data includes data include only temperature maps based on the first two surveys. Planck Collaboration XVI (2014) shows the very good consistency of cosmological models derived from intensity only with polarization data at small scale scales (high CMB multipoles). However, as detailed in Planck Collaboration VI (2014) (see their Fig. 27), the 2013 polarization data are known to be affected by systematic effects at low multipoles which were not

yet fully corrected, and thus these data were not used for cosmology. We have been careful to check that the results in this paper are robust with respect to these systematics. The error-bars we quote include uncertainties associated with residual systematics as estimated by repeating the analysis on different subsets of the data. We have also checked our data analysis on the latest version of the maps available to the consortium to check that the results we find are consistent within the error-bars quoted in this paper. The full mission maps for intensity as well as for polarization will be made publicly available in the fall of 2014.

2.1.2. Systematic effects in polarization

Current *Planck* polarization data are contaminated by a small amount of leakage from intensity to polarization, mainly due to bandpass mismatch (BPM) and calibration mismatch between detectors (Planck Collaboration Int. XIX 2014; Planck Collaboration VI 2014; Planck Collaboration III 2014). The BPM results from slight differences in the spectral response to Galactic emission of the polarization sensitive bolometers (PSB) (Planck Collaboration VI 2014). In addition, the signal differences leak into polarization. The calibration uncertainties translate into a small mismatch in the response of the detectors, which produces a signal leakage from intensity to polarization. As the microwave sky is dominated by the large scale emission from the Galaxy and the CMB dipole, systematics affect the polarization maps mainly on large angular scales. We were only able to correct the maps for leakage of Galactic emission due to bandpass mismatch.

The observed Stokes Q_{ν}^{obs} and U_{ν}^{obs} maps at a given frequency ν can be written as,

$$Q_{\nu}^{\text{obs}} = Q^c + Q_{\nu}^G + Q^n + L_{\nu}^G(I \rightarrow Q), \quad (1)$$

$$U_{\nu}^{\text{obs}} = U^c + U_{\nu}^G + Q^n + L_{\nu}^G(I \rightarrow U), \quad (2)$$

where the term L^G corresponds to the BPM leakage map for Galactic emission, which is computed using the coupling coefficient of each detector to the sky emission spectrum together with the actual sky scanning strategy. The superscript c represents the CMB polarization, n represents the noise and the index G incorporates all the Galactic emission components in intensity at *Planck* frequencies. We restrict our analysis to intermediate Galactic latitudes where the dominant Galactic emission at HFI frequencies is dust emission. The polarized HFI maps we used are corrected for the dust BPM, to a first approximation, using sky measurements of the spectral transmission of each bolometer (Planck Collaboration IX 2014). At LFI frequencies, we correct for BPM coming from the low frequency Galactic components, i.e., the AME, synchrotron and free-free emission (Planck Collaboration III 2014), using sky measurements of the spectral transmission of each bolometer.

To test the results presented in this paper for systematic effects, we use multiple data sets that include the maps made with two independent groups of four PSBs (detector sets “DS1” and “DS2”, see Table 3 in Planck Collaboration VI 2014), the half-ring maps (using the first or second halves of the data from each stable pointing period, “HR1” and “HR2”) and maps made with individual sky surveys (“S1”, “S2”, etc.). The HR1 and HR2 maps are useful to assess the impact on our data analysis of the noise and systematic effects on scales smaller than $20'$. The maps made with individual sky surveys are useful to quantify the impact of systematic effects on larger angular scales, particularly from beam ellipticity and far sidelobes (Planck Collaboration III 2014; Planck Collaboration VI 2014). For the intensity data, we

² <http://healpix.jpl.nasa.gov>

Table 1. Summary of *Planck*, *WMAP* and ancillary data used in this paper for both intensity and polarization.

Telescope/Survey	Frequency [GHz]	Resolution [arcmin]	Reference
Haslam	0.408	60	Haslam et al. (1982)
WMAP 9-year . . .	23	48.42	Bennett et al. (2013)
Planck	28.4	32.23	Planck Collaboration I (2014)
WMAP 9-year . . .	33	37.44	Bennett et al. (2013)
WMAP 9-year . . .	41	28.62	Bennett et al. (2013)
Planck	44.1	27.01	Planck Collaboration I (2014)
WMAP 9-year . . .	61	19.56	Bennett et al. (2013)
Planck	70.4	13.25	Planck Collaboration I (2014)
WMAP 9-year . . .	94	12.30	Bennett et al. (2013)
Planck	100	9.65	Planck Collaboration I (2014)
Planck	143	7.25	Planck Collaboration I (2014)
Planck	217	4.99	Planck Collaboration I (2014)
Planck	353	4.82	Planck Collaboration I (2014)
Planck	545	4.68	Planck Collaboration I (2014)
Planck	857	4.32	Planck Collaboration I (2014)
DIRBE	3000	50	Hauser et al. (1998)
H α		60	Dickinson et al. (2003)
LAB H I		36	Kalberla et al. (2005)

use the first two surveys S1 and S2, whereas for polarization we use the first four surveys grouped into odd (S1+S3) and even (S2+S4) pairs because they share the same scanning strategy.

The different data sets are independent observations of the same sky that capture noise and systematic effects. They provide means to assess the validity and self-consistency of our analysis of the *Planck* data. The different map combinations highlight different systematic effects on various timescales and across different dimensions.

- Half-ring maps share the same scanning strategy and detectors so they have the same leakage from intensity to polarization. The difference between these two maps shows the noise that is not correlated. The removal of glitches induce some noise correlation between the two half-ring maps that affects the data at all multipoles.
- Surveys 1 and 3 (respectively, 2 and 4) also share the same scanning strategy. The differences between odd and even surveys show all systematic effects associated with the scanning strategy.
- Detector set maps have the same combination of scans. The difference between detector set maps show all systematic effects associated with specific detectors.

An additional method allows us to test our results against systematic effects at low multipole (ℓ) from calibration mismatch. We use the bandpass filter shown in Fig. 1, which is constructed using the recipe discussed in Marinucci et al. (2008). The structures in the Stokes Q and U maps are filtered out at low and high multipoles ($\ell < 32$ and $\ell > 256$). The choice of $\ell_{\min} = 32$ is guided by the presence of systematic effects at large scales, whereas $\ell_{\max} = 256$ is fixed by the resolution of the data and the HEALPix pixel resolution used in our analysis (see Sect. 4.4). We repeat the data analysis with the filtered data and compare the results (Sect. 8.2).

2.2. WMAP data

We use the *WMAP* nine year data (Bennett et al. 2013) from the Legacy Archive for Microwave Background Data Analysis

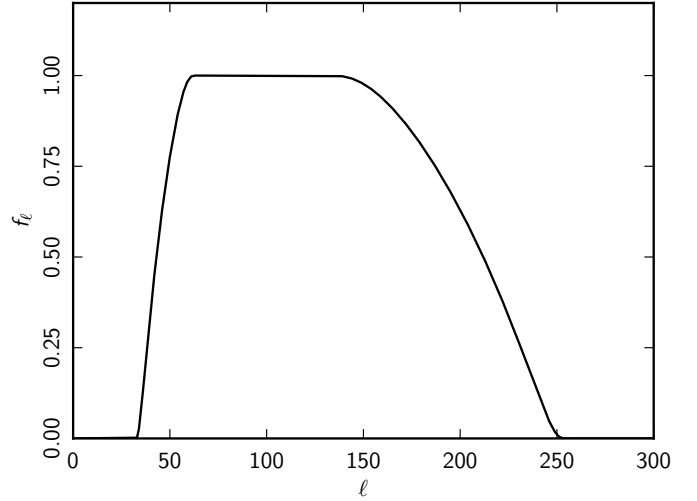


Fig. 1. Filter response used to obtain the filtered Stokes Q and U maps, which we use to test our results against data systematic effects (Sect. 2.1.2).

(LAMBDA)³ provided in the HEALPix pixelization scheme with a resolution $N_{\text{side}} = 512$. *WMAP* observed the sky in five frequency bands, denoted K, Ka, Q, V, and W, centred at the frequencies 23, 33, 41, 61, and 94 GHz, respectively. *WMAP* has ten differencing assemblies (DAs), one for both K and Ka bands, two for Q band, two for V band, and four for W band. *WMAP* has frequency-dependent resolution, ranging from 52' (K band) to 12' (W band). Multiple DAs at each frequency for Q, V and W bands are combined using simple average to generate a single map per frequency band.

WMAP also released temperature and polarization data for each of the individual nine years of observation. To assess the impact of *WMAP* noise and systematic effects on our results, we perform the data analysis with each of the nine individual years of data.

³ <http://lambda.gsfc.nasa.gov>

2.3. Ancillary data

We complement the *Planck* and *WMAP* data with several ancillary sky maps. We use the 408 MHz map from Haslam et al. (1982), and H α map from Dickinson et al. (2003) (hereafter DDD) as tracers of synchrotron and free-free emission, respectively. No dust extinction correction ($f_d = 0.0$) has been applied to the DDD H α map, which is expressed in units of Rayleigh (R). For our simulations we use the Leiden/Argentine/Bonn (LAB) survey of Galactic HI column density (Kalberla et al. 2005) as a tracer of dust emission (Planck Collaboration XXIV 2011; Planck Collaboration Int. XVII 2014). Finally, we use the DIRBE 100 μ m sky map to determine the dust temperature, like in Planck Collaboration XI (2014).

The 408 MHz, LAB HI, and DIRBE 100 μ m data are downloaded from LAMBDA. We use the DIRBE data corrected for ZLE. We project the DIRBE 100 μ m map on a HEALPix grid at $N_{\text{side}} = 512$ with a Gaussian interpolation kernel that reduces the angular resolution to 50'. Both the 408 MHz and the DDD H α maps are provided at 1° resolution. The LAB HI survey and DIRBE 100 μ m data have angular resolutions of 36' and 50', respectively.

3. Global mask

In the data analysis we use a global mask, shown in Fig. 2, which selects regions of dust emission from the ISM at intermediate Galactic latitudes. We only want to study polarization in regions where thermal dust emission dominates. This means that we need to remove the area around the Galactic plane, where other Galactic contributions are significant, and remove the high latitude regions, where the anisotropies of the cosmic infrared background (CIB) are important with respect to dust emission. The global mask combines thresholds on several sky emission components (in intensity): carbon monoxide (CO) line emission; free-free; synchrotron; the CIB anisotropies; and point sources. We now detail how the global mask is defined.

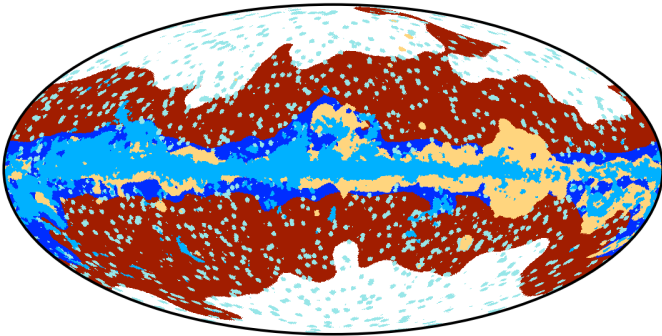


Fig. 2. Global mask used in the cross-correlation (CC) analysis (Mollweide projection in Galactic coordinates). It comprises the CIB mask (white region), the CO mask (light-blue), the free-free mask (beige), the Galactic mask (deep-blue), and the mask of point sources (turquoise). We use the red regions of the sky. We refer readers to Sect. 3 for a detailed description of how the global mask is defined.

In the regions of lowest dust column density at high Galactic latitudes, brightness fluctuations from the CIB are significant. To define the CIB mask, we apply a threshold on the ratio between the root mean square (rms) of the total Galactic emission and of

the CIB at 353 GHz:

$$\left| \frac{\sigma_G}{\sigma_{\text{CIB}}} \right| < 9, \quad (3)$$

where σ_G and σ_{CIB} are defined as

$$\sigma_{\text{CIB}}^2 = \sum_{\ell} \frac{2\ell + 1}{4\pi} C_{\ell}^{\text{CIB}} b_{\ell}^2 w_{\ell}^2, \quad (4)$$

$$\sigma_c^2 = \sum_{\ell} \frac{2\ell + 1}{4\pi} C_{\ell}^c b_{\ell}^2 w_{\ell}^2, \quad (5)$$

$$\sigma_G^2 = \sigma^2(I_{353}) - \sigma_c^2 - \sigma_{\text{CIB}}^2. \quad (6)$$

For this threshold, the CIB contribution to the CC coefficients in Sect. 4.2 is smaller than about 1% ($1/9^2$) of that of the total Galactic emission at 353 GHz. The summation is over the multipole range $15 < \ell < 300$ (corresponding to an effective range of angular scales from 1° to 10°). C_{ℓ}^{CIB} is the best-fit CIB power spectrum at 353 GHz (Planck Collaboration XXX 2014), C_{ℓ}^c is the best-fit CMB power spectrum (Planck Collaboration XV 2014), I_{353} represents the *Planck* 353 GHz map, b_{ℓ} is the beam function and w_{ℓ} is the HEALPix pixel window function. We measure the Galactic to CIB emission ratio over patches with 10° radius centred on HEALPix pixels at a resolution $N_{\text{side}} = 32$.

The CO, free-free, and synchrotron emission are more important close to the Galactic plane. The first three CO line transitions $J = 1 \rightarrow 0$, $J = 2 \rightarrow 1$, and $J = 3 \rightarrow 2$ at 115, 230, and 345 GHz, respectively, are significant emission components in the *Planck* intensity maps (Planck Collaboration XIII 2014). The CO mask is defined by applying a threshold of 1 K km s⁻¹ on the “Type 2” CO $J = 1 \rightarrow 0$, which is extracted using the *Planck* data between 70 and 353 GHz (Planck Collaboration XIII 2014). The free-free emission is weak compared to the CO line emission at 100 GHz for most molecular clouds. In massive star-forming regions and for the diffuse Galactic plane emission, free-free emission is significant (Planck Collaboration Int. XIV 2014). We take the *WMAP* maximum entropy method free-free map (Bennett et al. 2013) at 94 GHz and apply a threshold of 10 μ K_{RJ} (in Rayleigh-Jeans temperature units) to define the free-free mask. In addition, we use the Galactic mask (CS-CR75) from the *Planck* component separation results (Planck Collaboration XII 2014) to exclude the synchrotron emission from the Galactic plane and the Galactic “haze” (Planck Collaboration Int. IX 2013). We also apply the *Planck* point source mask (Planck Collaboration XV 2014).

Our mask focuses on the part of the sky where dust is the dominant emission component at HFI frequencies. This choice makes the spectral leakage from free-free and CO line emissions to polarization maps negligible. After masking we are left with 39% of the sky at intermediate Galactic latitudes ($10^\circ < |b| < 60^\circ$). The same global mask is used for both intensity and polarization correlation analysis to compare results over the same sky.

4. Cross-correlation method

We use the CC analysis adopted in many studies (Banday et al. 1996; Gorski et al. 1996; Davies et al. 2006; Page et al. 2007; Ghosh et al. 2012; Planck Collaboration Int. XII 2013) to extract the signal correlated with the 353 GHz template in intensity and polarization. The only underlying assumption is that the spatial structure in the 353 GHz template and in the map under analysis are locally correlated. To reduce this assumption, we apply the CC analysis locally over patches of sky of

10° radius (Sect. 4.4). Our choice for the dust template is presented in Sect. 4.1. The methodology is introduced for intensity in Sect. 4.2 and for polarization in Sect. 4.3. The practical implementation of the method is outlined in Sect. 4.4.

4.1. 353 GHz template

We perform the CC analysis locally in the pixel domain using the *Planck* 353 GHz maps of Stokes parameters as representative internal templates for dust emission in intensity (I with the ZLE subtracted) and polarization (Q and U). Our choice of a *Planck* map as a dust template addresses some of the issues plaguing alternative choices. First, unlike the H I map, the 353 GHz map traces the dust in both H I and H₂ gas (Reach et al. 1998; Planck Collaboration XXIV 2011; Planck Collaboration Int. XVII 2014). Second, unlike the full-sky Finkbeiner et al. (1999) 94 GHz (hereafter FDS) map, the 353 GHz map does not rely on an extrapolation over a large frequency range, from 100 μ m to the *Planck* bands. The main drawback of the 353 GHz template is that it includes CMB and CIB anisotropies. By introducing the global mask, we work with the sky region where the CIB anisotropies are small compared to dust emission. However, the contribution of the CMB to the CC coefficients, most significant at microwave frequencies, needs to be subtracted.

4.2. Intensity

4.2.1. Correlation with the 353 GHz template

For the intensity data, the CC coefficient (α_ν^I) is obtained by minimizing the χ_1^2 expression given by,

$$\chi_1^2 = \sum_{k=1}^{N_{\text{pix}}} [I_\nu(k) - [\alpha_\nu^I]_{353}^{1T} I_{353}(k) - a]^2, \quad (7)$$

where I_ν and I_{353} denote the data and the 353 GHz template maps, respectively. This is a linear fit and the solution is computed analytically. Here the CC coefficient is a number in K_{CMB} K_{CMB}^{-1} , as both I_ν and I_{353} are expressed in K_{CMB} units. The constant offset, a , takes into account the local mean present in the template as well as in the data. The sum is over the unmasked pixels, k , within a given sky-patch. We are insensitive to the residual dipole present at *Planck* frequencies because we perform local correlation over 10° radius patches. The index ‘1T’ represents the 353 GHz correlated coefficient at a given frequency ν that we obtained using one template only.

The CC coefficient at a given frequency includes the contribution from all the emission components that are correlated with the 353 GHz template (Appendix A). It can be decomposed into the following terms:

$$[\alpha_\nu^I]_{353}^{1T} = \alpha^I(c_{353}^I) + \alpha_\nu^I(d_{353}) + \alpha_\nu^I(s_{353}) + \alpha_\nu^I(f_{353}) + \alpha_\nu^I(a_{353}), \quad (8)$$

where c_{353}^I , d_{353} , s_{353} , f_{353} , and a_{353} refer to the CMB, dust, synchrotron, free-free, and AME signals that are correlated with the 353 GHz template, respectively. The CMB CC coefficient term is achromatic because Eq. 8 is expressed in K_{CMB} units. We neglect the contributions of the three CO lines, point sources, and the CIB anisotropies, since these are subdominant within our global mask (Sect. 3). We also neglect the cross-correlation of the ZLE with the dust template. The chance correlations between the emission components we neglect and the dust template contribute to the statistical uncertainties on the dust SED,

but do not bias it. We checked this with Monte Carlo simulations (Appendix B) and by repeating our analysis on HFI maps with the ZLE subtracted. The correlation terms of the synchrotron and AME components are negligible at $\nu \geq 100$ GHz, as synchrotron and AME both have a steep spectrum that falls off fast at high frequencies. The free-free emission is weak outside the Galactic plane at high frequencies and does not contribute significantly to the CC coefficients. The synchrotron, AME and free-free terms only become significant at $\nu < 100$ GHz inside our global mask.

4.2.2. Correlation with two and three templates

To remove $\alpha_\nu^I(s_{353})$ and $\alpha_\nu^I(f_{353})$ in Eq. 8, we cross-correlate the *Planck* and *WMAP* data with either two or three templates (including the dust template). We use the 353 GHz and the 408 MHz maps for the fit with two templates, and add the DDD H α map for the three-template fit. The χ_1^2 expressions that we minimize for these two cases are

$$\chi_1^2 = \sum_{k=1}^{N_{\text{pix}}} [I_\nu(k) - [\alpha_\nu^I]_{353}^{2T} I_{353}(k) - [\alpha_\nu^I]_{0.408}^{2T} I_{0.408}(k) - a]^2, \quad (9)$$

$$\chi_1^2 = \sum_{k=1}^{N_{\text{pix}}} [I_\nu(k) - [\alpha_\nu^I]_{353}^{3T} I_{353}(k) - [\alpha_\nu^I]_{0.408}^{3T} I_{0.408}(k) - [\alpha_\nu^I]_{\text{H}\alpha}^{3T} I_{\text{H}\alpha}(k) - a]^2, \quad (10)$$

where I_ν , I_{353} , $I_{0.408}$, and $I_{\text{H}\alpha}$ denote the data at a frequency ν , the *Planck* 353 GHz, Haslam 408 MHz, and DDD H α maps, respectively. For these multiple template fits, the CC coefficients are given by

$$[\alpha_\nu^I]_{353}^{2T} = \alpha^I(c_{353}^2) + \alpha_\nu^I(d_{353}) + \alpha_\nu^I(f_{353}) + \alpha_\nu^I(a_{353}) \quad (11)$$

$$[\alpha_\nu^I]_{353}^{3T} = \alpha^I(c_{353}^3) + \alpha_\nu^I(d_{353}) + \alpha_\nu^I(a_{353}). \quad (12)$$

The indices ‘2T’ and ‘3T’ are used here to distinguish the CC coefficients for the fit with two and three templates, respectively. The use of additional templates removes the corresponding terms from the right hand side of these equations. Equation 12 is used to derive the mean dust SED in intensity. Equations 8, 11, and 12 may be combined to derive $\alpha_\nu^I(s_{353})$ and $\alpha_\nu^I(f_{353})$.

4.3. Polarization

For the polarization data, we cross-correlate both the Stokes Q and U 353 GHz templates with the Q and U maps for all *Planck* and *WMAP* frequencies. Ideally in CC analysis, the template is free from noise, but the *Planck* 353 GHz polarization templates do contain noise, which may bias the CC coefficients. To circumvent this problem, we use two independent Q and U maps made with the two detector sets DS1 and DS2 at 353 GHz as templates (Sect. 2.1.2). The maps made with each of the two detector sets have independent noise and dust BPM. Using two polarization detector sets at 353 GHz with independent noise realizations reduces the noise bias in the determination of the 353 GHz CC coefficients. We use the detector set maps rather than the half-ring maps because the removal of glitches induces some noise correlation between the two half-ring maps that affects the data at all multipoles (Planck Collaboration VI 2014; Planck Collaboration X 2014).

The polarization CC coefficient (α_v^p) is derived by minimizing the χ_P^2 expression given by

$$\chi_P^2 = \sum_{i=1}^2 \sum_{k=1}^{N_{\text{pix}}} \left[Q_v(k) - [\alpha_v^p]_{353}^{1T} Q_{353}^i(k) - a \right]^2 + \left[U_v(k) - [\alpha_v^p]_{353}^{1T} U_{353}^i(k) - b \right]^2, \quad (13)$$

where the index i takes the values 1 and 2, which correspond to the DS1 and DS2 maps at 353 GHz. The summation k is over the unmasked pixels within a given sky-patch. The constant offsets a and b take into account the local mean present in the template as well as in the data Stokes Q and U maps, respectively. At 353 GHz, we cross-correlate the DS1 and DS2 maps of Q and U among themselves, minimizing

$$\chi_P^2 = \sum_{i=1}^2 \sum_{k=1}^{N_{\text{pix}}} \left[Q_{353}^j(k) - [\alpha_{353}^p]_{353}^{1T} Q_{353}^i(k) - a \right]^2 + \left[U_{353}^j(k) - [\alpha_{353}^p]_{353}^{1T} U_{353}^i(k) - b \right]^2. \quad (14)$$

The CC coefficients, α_v^p , comprise the contributions of CMB, dust, synchrotron and possibly AME polarization. The free-free polarization is expected to be negligible theoretically (Rybicki & Lightman 1979) and has been constrained to a few percent observationally (Macellari et al. 2011). The polarization decomposition is given by

$$[\alpha_v^p]_{353}^{1T} = \alpha^p(c_{353}^1) + \alpha_v^p(d_{353}) + \alpha_v^p(s_{353}) + \alpha_v^p(a_{353}). \quad (15)$$

The polarized CMB CC coefficient, $\alpha^p(c_{353}^1)$, is achromatic because Eq. 15 is expressed in K_{CMB} units. Unlike for intensity, due to the absence of any polarized synchrotron template free from Faraday rotation (Gardner & Whiteoak 1966), we cannot perform a fit with two templates to remove $\alpha_v^p(s_{353})$ in Eq. 15.

We have performed Monte Carlo simulations at the HFI frequencies in order to estimate the uncertainty on the CC coefficient induced by the noise and other Galactic emission present in the data (see Appendix B).

4.4. Implementation

Here we describe how we implement the CC method. The *Planck*, *WMAP*, HI and DIRBE sky maps are smoothed to a common resolution of 1° , taking into account the effective beam response of each map, and reduced to a HEALPix resolution $N_{\text{side}} = 128$. For the *Planck* and *WMAP* maps, we use the effective beams defined in multipole space that are provided in the *Planck* Legacy Archive⁴ (PLA) and LAMBDA website (Planck Collaboration VII 2014; Planck Collaboration IV 2014; Bennett et al. 2013). The Gaussian approximation of the average beam widths for *Planck* and *WMAP* maps are quoted in Table 1. For the HI and DIRBE maps, we also use Gaussian beams with the widths given in Table 1. For the polarization data, we use the “ismoothing” routine of HEALPix that decomposes the Q and U maps into E and B a_{rms} , applies Gaussian smoothing of 1° in harmonic space (after deconvolving the effective azimuthally symmetric beam response for each map), and transforms the smoothed E and B a_{rms} back into Q and U maps at $N_{\text{side}} = 128$ resolution.

We divide the intermediate Galactic latitudes into sky-patches with 10° radius centred on HEALPix pixels for $N_{\text{side}} = 8$.

For a much smaller radius we would have too few independent sky pixels within a given sky-patch to measure the mean dust SED. For a much larger radius we would have too few sky-patches to estimate the statistical uncertainty on the computation of the mean dust SED. Each sky-patch contains roughly 1500 pixels at $N_{\text{side}} = 128$ resolution. We only consider 400 sky-patches (N_{bins}), which have 500 or more unmasked pixels. We then cross-correlate the 353 GHz *Planck* internal template with the *WMAP* and *Planck* maps between 23 and 353 GHz, locally in each sky-patch to extract the 353 GHz correlated emission in intensity, along with its polarization counterpart. The sky-patches used are not strictly independent. Each sky pixel is part of a few sky-patches, which is required to sample properly the spatial variations of the CC coefficients. The mean number of times each pixel is used in CC coefficients (N_{visit}) is estimated with the following formula:

$$N_{\text{visit}} = \frac{N_{\text{bins}} \times \langle N_{\text{pixels}} \rangle}{0.39 \times N_{\text{total}}} \sim 5, \quad (16)$$

where $N_{\text{total}} = 12 \times N_{\text{side}}^2$ is the total number of pixels at 1° resolution, 0.39 is the fraction of the sky used in our analysis and $\langle N_{\text{pixels}} \rangle = 1000$ is the average number of pixels per sky-patch after masking.

5. Component separation methodology

At the highest frequencies ($\nu \geq 100$ GHz) within our mask, the two main contributors to the CC coefficient are the CMB and dust emission. In this section, we detail how we separate them and estimate the spectral index of the dust emission (β_d) in intensity and polarization.

5.1. Separation of dust emission

The CC coefficients at $\nu \geq 100$ GHz can be written as

$$[\alpha_v]_{353}^{1T} = \alpha(c_{353}^1) + \alpha_v(d_{353}), \quad (17)$$

where c_{353}^1 and d_{353} are the 353 GHz correlated CMB and dust emission, respectively. Equation 17 holds for both intensity and polarization analysis. The CMB CC coefficient is achromatic in K_{CMB} units, i.e., in temperature units relative to the CMB blackbody spectrum. To remove the CMB contribution, we work with the differences of CC coefficients between two given frequencies. To measure the dust spectral index both in intensity and polarization, we choose to work with colour ratios defined between two given frequencies ν_2 and ν_1 as

$$R_{\nu_0}(\nu_2, \nu_1) = \frac{[\alpha_{\nu_2}]_{353}^{1T} - [\alpha_{\nu_0}]_{353}^{1T}}{[\alpha_{\nu_1}]_{353}^{1T} - [\alpha_{\nu_0}]_{353}^{1T}} = \frac{\alpha_{\nu_2}(d_{353}) - \alpha_{\nu_0}(d_{353})}{\alpha_{\nu_1}(d_{353}) - \alpha_{\nu_0}(d_{353})}, \quad (18)$$

where ν_0 represents the reference CMB frequency which is chosen to be 100 GHz in the present analysis. To convert the measured colour ratio into β_d we follow earlier studies (Planck Collaboration Int. XVII 2014; Planck Collaboration XI 2014) by approximating the SED of the dust emission with a modified blackbody (MBB, hereafter) spectrum (Planck Collaboration XXV 2011; Planck Collaboration XXIV 2011; Planck Collaboration XI 2014) given by

$$\alpha_v(d_{353}) = F_\nu C_\nu A_d \nu^{\beta_d} B_\nu(T_d), \quad (19)$$

⁴ <http://archives.esac.esa.int>

where T_d is the colour temperature and β_d is the spectral index of the dust emission. The factor F_ν takes into account the conversion from MJy sr⁻¹ (with the photometric convention $\nu I_\nu = \text{constant}$) to K_{CMB} units, while C_ν is the colour correction that depends on the value of β_d and T_d . The colour correction is computed knowing the bandpass filters at the HFI frequencies (Planck Collaboration IX 2014) and the spectrum of the dust emission. Using Eq. 19, the colour ratio can be written as a function of β_d and T_d :

$$R_{\nu_0}(\nu_2, \nu_1) = \frac{F_{\nu_2} C_{\nu_2} \nu_2^{\beta_d} B_{\nu_2}(T_d) - F_{\nu_0} C_{\nu_0} \nu_0^{\beta_d} B_{\nu_0}(T_d)}{F_{\nu_1} C_{\nu_1} \nu_1^{\beta_d} B_{\nu_1}(T_d) - F_{\nu_0} C_{\nu_0} \nu_0^{\beta_d} B_{\nu_0}(T_d)} = g(\beta_d, T_d). \quad (20)$$

In Sect. 6.1, we use the three *Planck* maps, at 100, 217, and 353 GHz, to compute $R_{100}(353, 217)$ and measure the dust spectral index ($\beta_{d,\text{mm}}^I$) at microwave frequencies (or mm wavelengths), for each sky-patch. In the next section, we explain how we determine T_d .

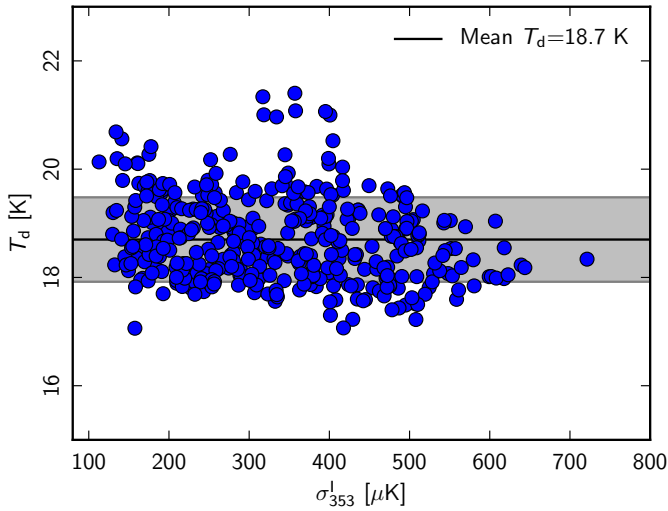


Fig. 3. Dust colour temperatures, T_d , computed from $R(3000, 857)$, are plotted versus the local dispersion of the 353 GHz intensity template, σ_{353}^I . The mean T_d is 18.7 K, with a standard deviation of 0.8 K across sky-patches (shaded area).

5.2. Measuring colour temperatures in intensity

The dust temperatures inferred from an MBB fit of the *Planck* at $\nu \geq 353$ GHz and the IRAS 100 μm sky maps at 5' resolution (Planck Collaboration XI 2014) cannot be used to compute mean temperatures within each sky-patch because the fits are non-linear. The two FIR frequencies, *Planck* 857 GHz and DIRBE 100 μm (3000 GHz), which are close to the dust emission peak, are well suited to measure T_d for each sky-patch. We use the *Planck* 353 GHz map as a template to compute the colour ratio $R^I(3000, 857)$ over each sky-patch, as described in Eq. 18. The superscript I on the colour ratio and β_d denote intensity. As the CMB signal is negligible at FIR frequencies, we work directly with the ratio $R^I(3000, 857)$, without subtracting the 100 GHz CC measure. We assume a mean dust spectral index at FIR frequencies, $\beta_{d,\text{FIR}}^I$, of 1.65. This mean value of $\beta_{d,\text{FIR}}^I$ was the one derived from the analysis of high Galactic latitude data (Planck

Collaboration Int. XVII 2014) and is consistent with the analysis of the whole sky (Planck Collaboration XI 2014). We use the colour ratio $R^I(3000, 857)$ and mean $\beta_{d,\text{FIR}}^I$ to estimate T_d values for each sky-patch by inverting the relation given in Eq. 20.

In Fig. 3, we plot the derived T_d versus the local brightness dispersion of the *Planck* 353 GHz template in intensity (σ_{353}^I). We point out that σ_{353}^I is not an uncertainty in the 353 GHz intensity template. The mean value of T_d over our mask at intermediate Galactic latitudes is 18.7 ± 0.8 K. This value is slightly smaller than the mean value at high Galactic latitudes, 19.8 K, measured using the dust-HI correlation in Planck Collaboration Int. XVII (2014). The difference comes from the fact that the two analyses probe different regions on the sky. Our estimate of mean $T_d = 18.7$ K using $\beta_{d,\text{FIR}}^I = 1.65$ at intermediate latitudes is consistent with the results from the all-sky analysis performed using the HFI *Planck* data (Planck Collaboration XI 2014).

Our T_d values are derived for a fixed $\beta_{d,\text{FIR}}^I$. To quantify the impact of this assumption, we also obtained T_d and $\beta_{d,\text{FIR}}^I$ values from a MBB fit to the dust emissivities at 100 μm and the *Planck* 353, 545 and 857 GHz frequencies, for each sky-patch. The T_d values from the MBB fits are closely correlated with T_d values determined using the ratio $R^I(3000, 857)$ and a fixed spectral index. Variations of the $\beta_{d,\text{FIR}}^I$ values just increases the scatter of the T_d values by about 20% due to the $\beta_{d,\text{FIR}}^I - T_d$ anti-correlation.

5.3. Separation of CMB emission in intensity

The CC coefficient, derived in Eq. 8, contains the CMB contribution that is achromatic in K_{CMB} units. We determine this CMB contribution assuming that the dust emission is well approximated by a MBB spectrum from 100 to 353 GHz. For each sky-patch, we use the values of $\beta_{d,\text{mm}}^I$ and T_d from Sects. 6.1 and 5.2. We solve for two parameters, the CMB contribution, $\alpha^I(c_{353}^I)$, and the dust amplitude, A_d^I , by minimizing

$$\chi_s^2 = \sum_\nu \left(\frac{[\alpha_\nu^I]_{353}^{IT} - \alpha^I(c_{353}^I) - F_\nu C_\nu A_d^I \nu^{\beta_{d,\text{mm}}^I} B_\nu(T_d)}{\sigma_{\alpha_\nu^I}} \right)^2, \quad (21)$$

where $\sigma_{\alpha_\nu^I}$ is the uncertainty on the CC coefficient, determined using the Monte Carlo simulations (Appendix B). The joint spectral fit of $\alpha^I(c_{353}^I)$, $\beta_{d,\text{mm}}^I$, T_d , and A_d^I leads to a degeneracy between the fitted parameters. To avoid this problem, we fix the values of $\beta_{d,\text{mm}}^I$ and T_d for each sky-patch based on the colour ratios, independent of the value of $\alpha^I(c_{353}^I)$. The CMB contributions are subtracted from the CC coefficients at all frequencies, including the LFI and WMAP data not used in the fit. After CMB subtraction, the CC coefficient ($\tilde{\alpha}_\nu^I$) for the 353 GHz template is

$$[\tilde{\alpha}_\nu^I]_{353}^{IT} = \alpha_\nu^I(d_{353}) + \alpha_\nu^I(a_{353}) + \alpha_\nu^I(f_{353}) + \alpha_\nu^I(s_{353}). \quad (22)$$

We perform the same exercise on the two- and three-template fits to derive the CMB subtracted CC coefficients.

6. Dust spectral index for intensity

Here we estimate the dust spectral index $\beta_{d,\text{mm}}^I$ at microwave frequencies ($\nu \leq 353$ GHz). We present the results of the data analysis and estimate the uncertainties, including possible systematic effects.

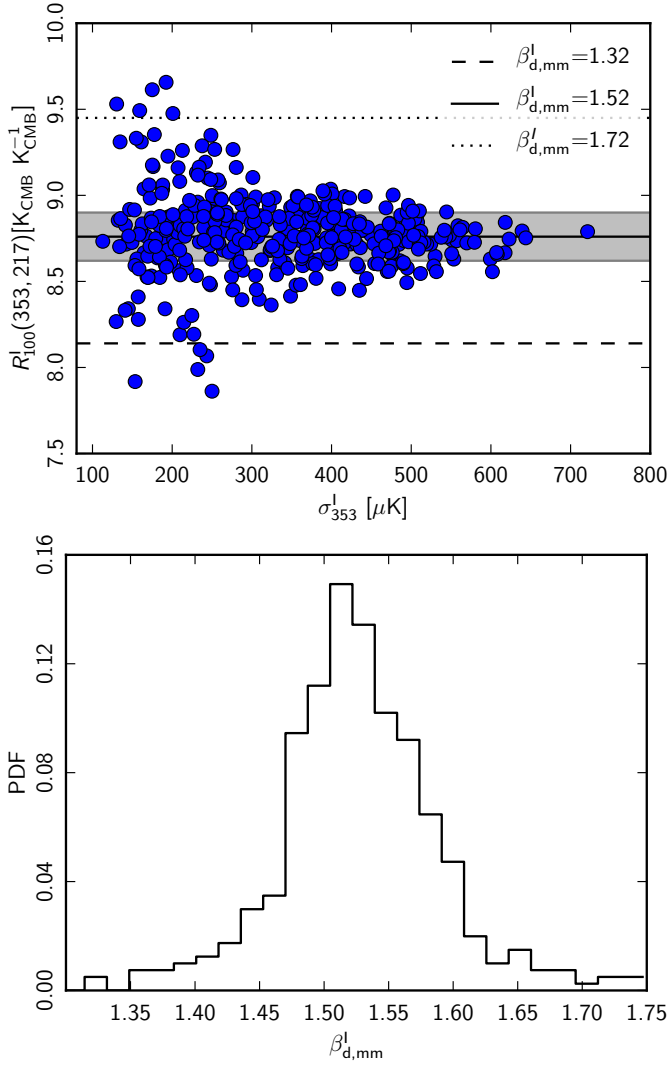


Fig. 4. *Top:* Colour ratio $R_{100}^I(353, 217)$ versus dispersion of the 353 GHz template σ_{353}^I for each sky-patch. The 1σ dispersion of the $R_{100}^I(353, 217)$ values is shown as the shaded grey area. The mean ratio corresponds to a spectral index of 1.52 (solid line) for a mean $T_d = 18.7$ K. *Bottom:* probability distribution function (PDF) of the $\beta_{d,mm}^I$ values derived from $R_{100}^I(353, 217)$ using the specific value of T_d for each sky-patch. The measured 1σ dispersion of $\beta_{d,mm}^I$ is 0.07.

6.1. Measuring $\beta_{d,mm}^I$

We use the three *Planck* maps, at 100, 217, and 353 GHz, to derive a mean $\beta_{d,mm}^I$, assuming an MBB spectrum of the dust emission (Sect. 5.1). The 217 and 353 GHz maps have the highest signal-to-noise ratio for dust emission at microwave frequencies, whereas 100 GHz map is used as a reference frequency to subtract the CMB contribution at the CC level. We estimate $R_{100}^I(353, 217)$ for each sky-patch using the relation given by Eq. 18. The values of $R_{100}^I(353, 217)$ are plotted in top panel of Fig. 4 as a function of σ_{353}^I , which allows us to identify the statistical noise and systematic effects due to uncertainties on the CC coefficients. Our Monte Carlo simulations (Appendix B) show that the uncertainties on $R_{100}^I(353, 217)$ scale approximately as the inverse square-root of σ_{353}^I , and that the scatter in the mea-

sured $R_{100}^I(353, 217)$ for sky-patches with low σ_{353}^I is due to data noise.

For each sky-patch, we derive $\beta_{d,mm}^I$ from $R_{100}^I(353, 217)$ by inverting Eq. 20 for the values of T_d derived in Sect. 5.2. The histogram of $\beta_{d,mm}^I$ for all sky-patches is presented in the bottom panel of Fig. 4. The 1σ dispersion of $\beta_{d,mm}^I$ is 0.07. The statistical uncertainty on the mean $\beta_{d,mm}^I$ is 0.01, which is computed from the 1σ deviation divided by the square root of the number of independent sky-patches ($400/N_{\text{visit}}$) used. This estimate of the statistical error bar on $\beta_{d,mm}^I$ takes into account the uncertainties associated with the chance correlation between the dust template and emission components (CO lines, point sources, the CIB anisotropies and the ZLE) not fitted with templates. It also includes uncertainties on the subtraction of the CMB contribution.

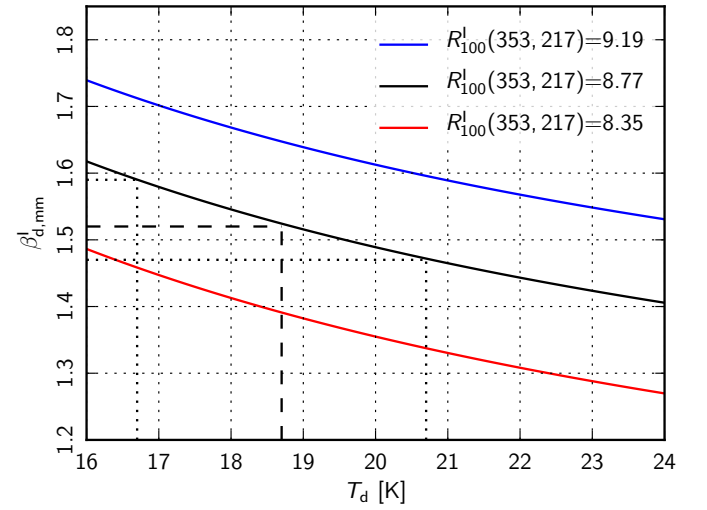


Fig. 5. Variation of $\beta_{d,mm}^I$ with T_d for constant values of $R_{100}^I(353, 217)$. The dashed line corresponds to a mean $T_d = 18.7$ K and $\beta_{d,mm}^I = 1.52$ for the best-fit value of $R_{100}^I(353, 217) = 8.77$. The two dotted line lines correspond to a change in T_d of ± 2 K about its mean value, resulting in change of $\beta_{d,mm}^I$ value of ± 0.05 .

6.2. Uncertainties on $\beta_{d,mm}^I$

To assess the systematic uncertainties on the mean spectral index, we repeat our CC analysis on maps made with subsets of the *Planck* data (Sect. 2.1.2), keeping the same ZLE-subtracted *Planck* 353 GHz map as a template. For each set of maps, we compute the mean $\beta_{d,mm}^I$ from $R_{100}^I(353, 217)$ values. Table 2 lists the derived $\beta_{d,mm}^I$ values. The multiple estimates allow us to determine the uncertainties on $\beta_{d,mm}^I$, including data systematic effects. We find a mean dust spectral index $\beta_{d,mm}^I = 1.52 \pm 0.02$ (syst.) ± 0.01 (stat.). We find that the spectral index of dust emission at microwave frequencies is slightly flatter than the mean index of 1.65 at FIR frequencies derived from MBB fits to the *Planck* data at $\nu \geq 353$ GHz in Planck Collaboration XI (2014).

Table 2. Dust spectral indices for intensity derived using multiple data sets (Sect. 2.1.2). We compute the systematic uncertainty on the mean $\beta_{\text{d,mm}}^{\text{I}}$ from the scatter of six measurements (three independent samples), which is 0.02.

Data sets	$\beta_{\text{d,mm}}^{\text{I}}$
S1	1.51
S2	1.50
Nominal HR1	1.52
Nominal HR2	1.52
Nominal DS1	1.50
Nominal DS2	1.56

6.3. Dependence of $\beta_{\text{d,mm}}^{\text{I}}$ on the choice of $\beta_{\text{d,FIR}}^{\text{I}}$

In Fig. 5 we plot $R_{100}^{\text{I}}(353, 217)$ as a function of $\beta_{\text{d,mm}}^{\text{I}}$ and T_{d} . The central black line corresponds to the median value of $R_{100}^{\text{I}}(353, 217)$ obtained using the CC analysis. Figure 5 shows that varying T_{d} by the observed 3σ deviation of ± 2 K from its mean value, changes $\beta_{\text{d,mm}}^{\text{I}}$ by ± 0.05 . To estimate $\beta_{\text{d,mm}}^{\text{I}}$, we use T_{d} , which in turn depends on $\beta_{\text{d,FIR}}^{\text{I}}$. If the value of $\beta_{\text{d,FIR}}^{\text{I}}$ increases from the value of 1.65 we have used, the mean value of T_{d} decreases, which in turn increases $\beta_{\text{d,mm}}^{\text{I}}$. A difference between $\beta_{\text{d,FIR}}^{\text{I}}$ and $\beta_{\text{d,mm}}^{\text{I}}$ is always present, independently of the starting value for $\beta_{\text{d,FIR}}^{\text{I}}$. Here and for the rest of the paper we focus on the difference between the two spectral indices, which does not depend on T_{d} .

6.4. Alternative approach of measuring $\beta_{\text{d,mm}}^{\text{I}}$

To derive the dust spectral index from $R_{100}^{\text{I}}(353, 217)$, we assume an MBB spectrum for the dust emission between 100 and 353 GHz (Sect. 5.1). To validate this assumption, we repeat our CC analysis with *Planck* maps corrected for CMB anisotropies using the CMB map from the spectral matching independent component analysis (SMICA, Planck Collaboration XII 2014). We infer $\beta_{\text{d,mm}}^{\text{I}}$ (SMICA) directly from the ratio between the 353 and 217 GHz CC coefficients without subtracting the 100 GHz CC coefficient, i.e.,

$$R_{\text{SMICA}}^{\text{I}}(353, 217) = \frac{[\alpha'_{353}]_{(353-\text{SMICA})}^{\text{IT}}}{[\alpha'_{217}]_{(353-\text{SMICA})}^{\text{IT}}}, \quad (23)$$

where α' refers to the CC coefficients computed with maps corrected for CMB anisotropies using the SMICA map. The histogram of the difference between the two sets of spectral indices $\beta_{\text{d,mm}}^{\text{I}}$ and $\beta_{\text{d,mm}}^{\text{I}}$ (SMICA) is presented in Fig. 6. The small mean difference of 0.02 is within the data uncertainties and systematic errors.

6.5. Comparison with other studies

Our determination of the spectral index $\beta_{\text{d,mm}}^{\text{I}}$ of the dust emission in intensity at intermediate Galactic latitudes may be compared with the results from similar analyses of the *Planck* data. In Planck Collaboration Int. XVII (2014), the CC analysis has been applied to the *Planck* data at high Galactic latitudes ($b < -30^\circ$) using an HI map as a dust template free from CIB and CMB anisotropies. This is a suitable template to derive the spectral dependence of dust emission at high Galactic latitudes. The same methodology of colour ratios has been used in

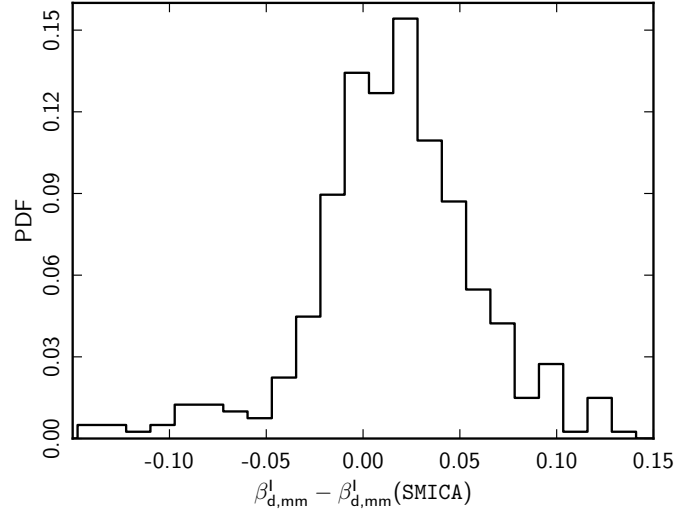


Fig. 6. Histogram of the difference between the spectral indices $\beta_{\text{d,mm}}^{\text{I}}$ from Eq. (20) and $\beta_{\text{d,mm}}^{\text{I}}$ (SMICA) from Eq. (23), where we applied the CC analysis to *Planck* maps corrected for CMB anisotropies with the SMICA CMB map.

that work. The mean dust spectral index, $\beta_{\text{d,mm}}^{\text{I}} = 1.53 \pm 0.03$, from Planck Collaboration Int. XVII (2014) is in good agreement with the mean value we find in this paper. In an analysis of the diffuse emission in the Galactic plane, the spectral index of dust at millimetre wavelengths is found to increase from $\beta_{\text{d,mm}}^{\text{I}} = 1.54$, for lines of sight where the medium is mostly atomic, to $\beta_{\text{d,mm}}^{\text{I}} = 1.66$, where the medium is predominantly molecular (Planck Collaboration Int. XIV 2014). The three studies indicate that the spectral index $\beta_{\text{d,mm}}^{\text{I}}$ is remarkably similar over the diffuse ISM observed at high and intermediate Galactic latitudes, and in the Galactic plane. Furthermore, in these three studies, $\beta_{\text{d,mm}}^{\text{I}}$ is found to be smaller than $\beta_{\text{d,FIR}}^{\text{I}}$, as derived in Planck Collaboration XI (2014).

7. Spectral energy distribution of dust intensity

In this section, we derive the mean SED of dust emission for intensity with its uncertainties from our CC analysis. The detailed spectral modelling of the dust SED is discussed in Sect. 7.2.

7.1. Mean dust SED

The mean SED is obtained by averaging the CC coefficients after CMB subtraction (see Sect. 5.3) over all sky-patches. The mean SED is expressed in K_{RJ} units, normalized to 1 at 353 GHz. The three SEDs obtained from the fit with one, two, and three templates are shown in Fig. 7. The SED values obtained with the three templates fit are listed in Table 3. The three SEDs are identical at the highest frequencies. They differ at $\nu < 100$ GHz due to the non-zero correlation between the 353 GHz dust template with synchrotron and free-free emission. At 23 GHz, after CMB correction the CC coefficient from the fit with three templates is lower by 10 and 35 % from those derived from the fits with two and one template, respectively. The 10 % difference accounts for the free-free emission correlated with dust and the 35 % difference for the combination of both synchrotron and free-free emission correlated with dust. At these low frequencies, the fit with three templates provides the best separation of the dust from the

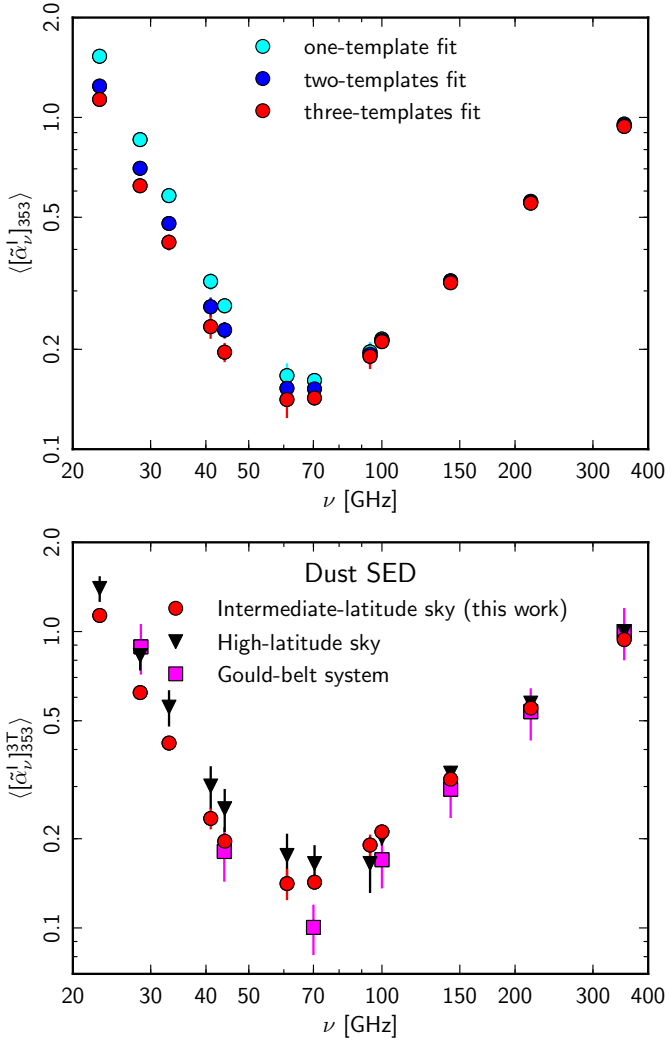


Fig. 7. *Top:* Mean SEDs normalized at 353 GHz obtained by averaging CC coefficients. These are CMB corrected, from the fits with one (cyan circles), two (blue circles) and three templates (red circles). The uncertainties at each frequency are estimated using the subsets of *Planck* and *WMAP* data. The three-templates fit provides the best separation of the dust emission from the synchrotron and free-free emission at $\nu < 100$ GHz. *Bottom:* For comparison, we show the dust SEDs normalized at 353 GHz presented in [Planck Collaboration Int. XVII \(2014\)](#) at high latitude (inverted triangles) and in [Planck Collaboration Int. XII \(2013\)](#) from the Gould Belt system (square symbol) together with the dust SED (red circles) derived in this paper.

synchrotron and free-free emission. It is this SED that we call the dust SED hereafter.

Our dust SED is similar to that of the Gould Belt system ([Planck Collaboration Int. XII 2013](#)) and high Galactic latitude sky ([Planck Collaboration Int. XVII 2014](#)). It shows the thermal dust emission at higher frequencies and is dominated by AME at lower, microwave, frequencies. At *WMAP* frequencies, our dust SED is similar to that obtained using the FDS 94 GHz map as a dust template in [Davies et al. \(2006\)](#) and [Ghosh et al. \(2012\)](#). The mean dust SED derived using the three-template fit depends on the correction of the DDD $H\alpha$ map for dust scattering and extinction ([Dickinson et al. 2003](#); [Witt et al. 2010](#); [Brandt & Draine 2012](#); [Bennett et al. 2013](#)). In Appendix C, we study the

impact of both assumptions on the mean dust SED, which are within a few percent at frequencies below 70 GHz and have no impact on frequencies above 100 GHz.

The total uncertainty on the dust SED includes the inter-calibration uncertainties on the data, the systematic uncertainties, the statistical uncertainties estimated from the variations of the CC coefficients across the sky-patches, and the uncertainties due to the CMB subtraction, as discussed for $\beta_{\text{d,mm}}^I$ in Sect. 6.1. The inter-calibration uncertainties (c_ν) for *Planck* and *WMAP* data are given in Table 3. To measure the systematic uncertainties, we repeat the CC analysis with the subsets of *WMAP* and *Planck* data, keeping the three templates fixed. We use the nine individual one-year maps from *WMAP*. For *Planck*, we use the two half-ring maps, as well as the Survey 1 and Survey 2 maps. The statistical uncertainties are computed from the 1σ dispersion of the CC coefficients over the 400 sky-patches divided by the square root of the number of independent sky-patches ($400/N_{\text{visit}}$). All four types of uncertainty, listed in Table 3, are added together in quadrature to compute the total uncertainty on the mean dust SED. They are shown in Fig. 7, but most do not appear because they are smaller than the size of the symbols.

7.2. Parametric modelling for intensity dust SED

A spectral fit of the dust SED is required to separate the thermal dust emission from the AME. We continue to use an MBB spectrum for the thermal dust emission, and consider three models with different spectra for the AME.

- Model DI+AI: In this first approach, we use the analytical model of the AME (AI) introduced by [Bonaldi et al. \(2007\)](#), which is a parabola in the $\log I_\nu$ – $\log \nu$ plane, parameterised by the peak frequency (ν_p) and the slope $-m_{60}$ at 60 GHz. The AME model (M_a) normalized at 23 GHz (in K_{RJ} units) is given by:

$$\log M_a = - \left(\frac{m_{60} \log \nu_p}{\log(\nu_p/60 \text{ GHz})} + 2 \right) \log \left(\frac{\nu}{23 \text{ GHz}} \right) + \frac{m_{60}}{2 \log(\nu_p/60 \text{ GHz})} \left[(\log(\nu/1 \text{ GHz}))^2 - (\log 23)^2 \right]. \quad (24)$$

This model is a good fit to spectra of dipole emission from small spinning dust particles computed with the SPDUST code ([Ali-Haïmoud et al. 2009](#); [Silsbee et al. 2011](#)). The second component is the MBB spectrum of the thermal dust emission derived from the high-frequency fits with $\beta_{\text{d,FIR}}^I = 1.65$. To account for the flattening for the dust SED below 353 GHz, we introduce a third component with a blackbody spectrum (BB). The BB spectrum is a good approximation of MDE from ferro-magnetic particles or magnetic inclusions in dust grains, as modelled by [Draine & Hensley \(2013\)](#), over this microwave frequency range. The mean T_d of the BB component (or MDE) is the same as that of MBB spectrum, which is 18.7 K. This combined dust model (DI) of MBB and BB emission is the same as that presented in [Planck Collaboration Int. XVII \(2014\)](#) for fitting the dust SED derived from the H I correlation. The total model is given in K_{RJ} units by:

$$\langle [\tilde{\alpha}_\nu^I]_{353}^{3T} \rangle = A_a^I M_a + \left[A_d^I \left(\frac{\nu}{353 \text{ GHz}} \right)^{\beta_{\text{d,FIR}}^I - 2} + A_b^I \left(\frac{\nu}{100 \text{ GHz}} \right)^{-2} \right] B_\nu(T_d), \quad (25)$$

Table 3. Mean microwave SEDs obtained from the fit with one, two, and three templates using the CC analysis.

Quantity	Experiment Frequency [GHz]											
	WMAP 23	Planck 28.4	WMAP 33	WMAP 41	Planck 44.1	WMAP 61	Planck 70.4	WMAP 94	Planck 100	Planck 143	Planck 217	Planck 353
$\langle [\tilde{a}_v^I]_{353}^{3T} \rangle$	1.1650	0.5964	0.4138	0.2350	0.1878	0.1413	0.1341	0.1811	0.2201	0.3097	0.5921	1.0000
σ_{stat}	0.0291	0.0163	0.0115	0.0067	0.0056	0.0037	0.0026	0.0034	0.0022	0.0025	0.0040	0.0062
σ_{sys}	0.0018	0.0102	0.0018	0.0014	0.0065	0.0028	0.0045	0.0023	0.0039	0.0035	0.0016	0.0011
c_v [%]	2.0	1.0	2.0	2.0	1.0	2.0	0.5	2.0	0.5	0.5	0.5	1.2
σ_{cmb}	0.0164	0.0079	0.0162	0.0159	0.0077	0.0151	0.0035	0.0133	0.0033	0.0025	0.0014	0.0006
σ_{tot}	0.0400	0.0215	0.0214	0.0179	0.0117	0.0160	0.0063	0.0143	0.0057	0.0052	0.0053	0.0113
S/N	29.2	27.7	19.4	13.1	16.0	8.8	21.4	12.7	38.6	60.0	111.4	88.1
C	1.0732	1.0000	1.0270	1.0480	1.0000	1.0450	0.9810	0.9924	1.0944	1.0210	1.1264	1.1170
U	0.9864	0.9487	0.9723	0.9577	0.9328	0.9091	0.8484	0.7998	0.7945	0.5917	0.3343	0.0751
$\langle [\tilde{a}_v^I]_{353}^{1T} \rangle$	1.5461	0.8079	0.5624	0.3165	0.2550	0.1641	0.1489	0.1838	0.2205	0.3087	0.5897	1.0000
σ_{tot}^{1T}	0.0579	0.0299	0.0249	0.0179	0.0124	0.0141	0.0063	0.0124	0.0052	0.0042	0.0049	0.0110
$\langle [\tilde{a}_v^I]_{353}^{2T} \rangle$	1.2653	0.6664	0.4667	0.2672	0.2169	0.1513	0.1415	0.1821	0.2201	0.3093	0.5906	1.0000
σ_{tot}^{2T}	0.0418	0.0224	0.0214	0.0169	0.0118	0.0144	0.0064	0.0128	0.0057	0.0049	0.0051	0.0110

$\langle [\tilde{a}_v^I]_{353}^{3T} \rangle$ \equiv mean dust SED in K_{RJ} units, normalized to 1 at 353 GHz, from the fit with three-templates. The values are not colour corrected.

σ_{stat} \equiv statistical uncertainty on the mean dust SED.

σ_{sys} \equiv systematic uncertainty on the mean dust SED.

c_v \equiv uncertainties on the inter-calibration [%] between *Planck* and *WMAP* frequencies (Planck Collaboration I 2014; Bennett et al. 2013).

σ_{cmb} \equiv uncertainty on the mean dust SED introduced by the CMB subtraction multiplied by the inter-calibration factor c_v .

σ_{tot} \equiv total uncertainty on the mean dust SED.

S/N \equiv signal-to-noise ratio on the mean dust SED.

C \equiv colour-correction factors computed with a linear combination of the power-law model and the MBB parameters listed in Table 4.

U \equiv unit conversion factors from thermodynamic (K_{CMB}) to Rayleigh-Jeans (K_{RJ}) temperature.

$\langle [\tilde{a}_v^I]_{353}^{1T} \rangle$ \equiv mean intensity SED in K_{RJ} units, normalized to 1 at 353 GHz, derived from the correlation of the maps with the one-template fit. The values are not colour corrected.

σ_{tot}^{1T} \equiv total uncertainty on the mean intensity SED with the one-template fit.

$\langle [\tilde{a}_v^I]_{353}^{2T} \rangle$ \equiv mean intensity SED in K_{RJ} units, normalized to 1 at 353 GHz, derived from the correlation of the maps with the two-template fit. The values are not colour corrected.

σ_{tot}^{2T} \equiv total uncertainty on the mean intensity SED with the two-template fit.

where the subscripts a, b, and d correspond to the AME, BB, and MBB components, respectively. The five free parameters of this model are m_{60} , ν_p , the amplitude of the AME (A_a^I), the amplitude of the BB component (A_b^I), and the amplitude of the MBB component (A_d^I). We fix $\beta_{d,FIR}^I = 1.65$ and $T_d = 18.7$ K, based on the measured $R^I(3000, 857)$, as discussed in Sect. 5.2.

- Model DII+AI: In this second approach, we use the same AME model as before, but without any BB component. To account for the flattening of the dust SED, we use the derived $\beta_{d,mm}^I$ (Sect. 6.2) for the MBB spectrum of the thermal dust emission (DII). The total model is given in K_{RJ} units by:

$$\langle [\tilde{a}_v^I]_{353}^{3T} \rangle = A_a^I M_a + A_d^I \left(\frac{\nu}{353 \text{ GHz}} \right)^{\beta_{d,mm}^I - 2} B_\nu(T_d), \quad (26)$$

where A_a^I is the amplitude of AME, A_d^I is the amplitude of thermal dust and $\beta_{d,mm}^I$ is the spectral index of thermal dust emission at microwave frequencies. We fix $\beta_{d,mm}^I = 1.52$ from Sect. 6.2 and $T_d = 18.7$ K from Sect. 5.2. The four free parameters of the model are the amplitudes of the AME and thermal dust components, plus m_{60} and ν_p . This model DII requires a change of the dust spectral index at 353 GHz to explain the transition between $\beta_d^I = 1.65$ in the FIR to 1.52 at microwave frequencies.

- Model DII+AII: In this third approach, the AME component (AII) is a linear combination of two spinning dust components arising from the typical cold neutral medium (CNM)

and warm neutral medium (WNM). In our analysis, we use the predicted SPDUST (v2) spectra (Ali-Haïmoud et al. 2009; Silsbee et al. 2011) of the CNM and WNM spinning dust components. Following the work of Hoang et al. (2011) and Ghosh et al. (2012), we shift both the WNM and CNM spectra in frequency space to fit the observed dust SED. The same DII model of the thermal dust emission is considered for this model. In this case, the spectral model is given in K_{RJ} units by:

$$\begin{aligned} \langle [\tilde{a}_v^I]_{353}^{3T} \rangle = & A_{WNM}^I D_{WNM}(\nu - \Delta\nu_{WNM}) \\ & + A_{CNM}^I D_{CNM}(\nu - \Delta\nu_{CNM}) \\ & + A_d^I \left(\frac{\nu}{353 \text{ GHz}} \right)^{\beta_{d,mm}^I - 2} B_\nu(T_d), \end{aligned} \quad (27)$$

where A_{WNM}^I is the amplitude of WNM spectrum normalized at 23 GHz, A_{CNM}^I is the amplitude of CNM spectrum normalized at 41 GHz, D_{WNM} is the SPDUST WNM spectrum, D_{CNM} is the SPDUST CNM spectrum, $\Delta\nu_{WNM}$ is the shift in the WNM spectrum, $\Delta\nu_{CNM}$ is the shift in the CNM spectrum, A_d^I and $\beta_{d,mm}^I$ are the amplitude and the spectral index of the thermal dust emission. We fix $\beta_{d,mm}^I = 1.52$ from Sect. 6.2 and $T_d = 18.7$ K from Sect. 5.2. The five free parameters of the model are the WNM amplitude, the WNM frequency shift, the CNM amplitude, the CNM frequency shift, and the amplitude of the MBB component.

The fits of the dust SED with models DI+AI, DII+AI, and DII+AII are shown in Fig. 8. The best fit model parameters are listed in Table 4.

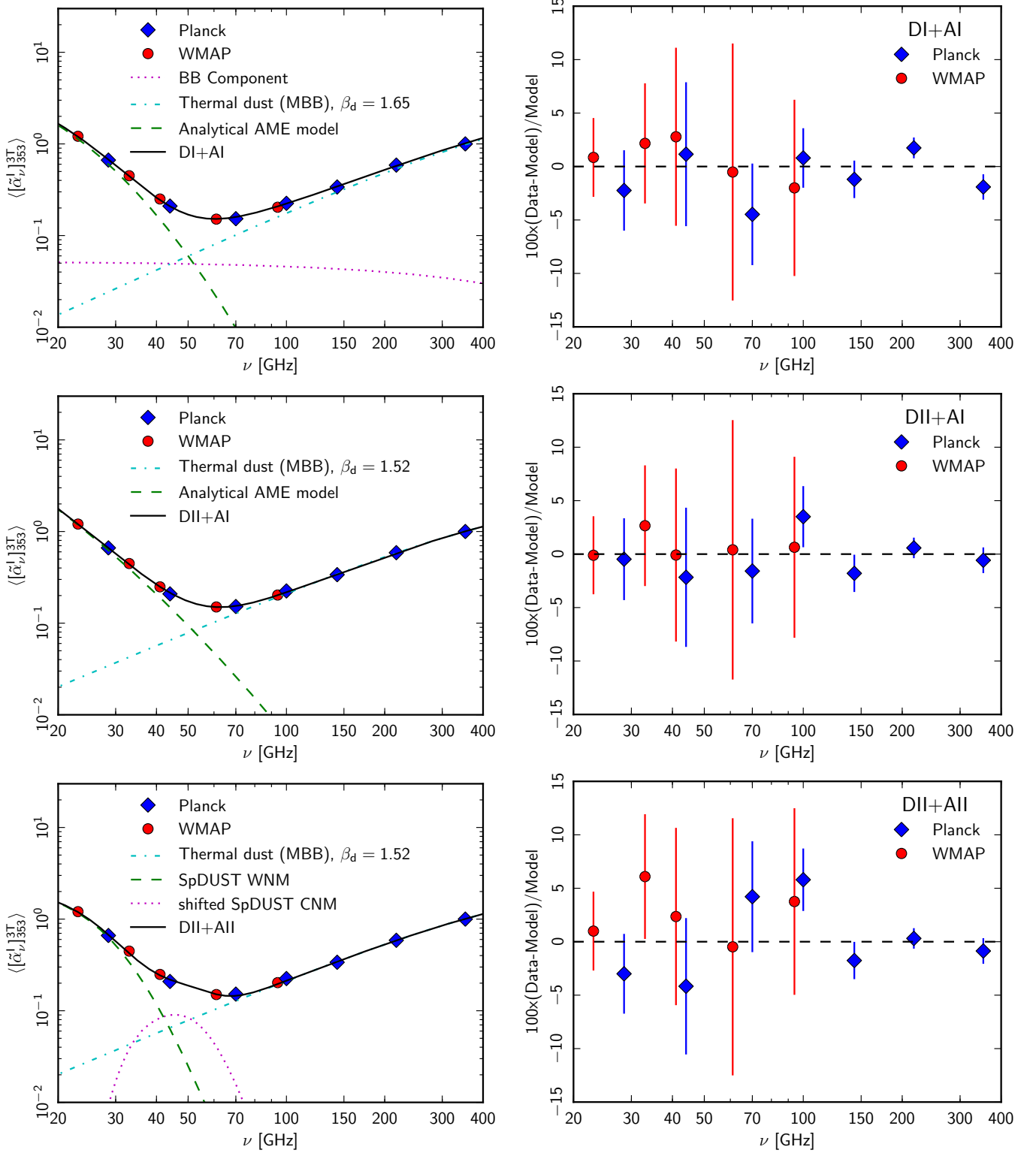


Fig. 8. Mean dust SED in K_{RJ} units, normalized to 1 at 353 GHz, with different spectral fits and the respective residuals. The three parametric model fits are DI+AI (top left), DII+AI (middle left), and DII+AII (bottom left), as presented in Sect. 7.2. Right: residuals after removing the best fit model listed in Table 4, from the mean dust SED. The three spectral models provide an equally good fit to the data, with residuals compatible with zero.

7.3. Astrophysical interpretation

The three spectral models DI+AI, DII+AI, and DII+AII provide equally good fits to the observed dust SED in intensity. We

discuss the astrophysical interpretation of the dust emission for each model.

In model DI, the spectral index of the thermal dust emission is constant from FIR to microwave frequencies. The change of

Table 4. Results of the spectral fits to the mean dust SED in intensity using *Planck* and *WMAP* maps.

Parameters	DI+AI	DII+AI	Parameters	DII+AI
A_d^I	$(22.44 \pm 0.28) \times 10^{-6}$	$(22.86 \pm 0.16) \times 10^{-6}$	A_d^I	$(22.93 \pm 0.16) \times 10^{-6}$
A_a^I	1.13 ± 0.04	1.18 ± 0.04	A_{WNM}^I	1.17 ± 0.04
ν_p [GHz] . . .	18.3 ± 3.8	9.7 ± 7.5	A_{CNM}^I	0.08 ± 0.02
m_{60}	3.42 ± 0.90	1.82 ± 0.41	$\Delta\nu_{\text{CNM}}$ [GHz] . . .	21.1 ± 2.7
A_b^I	$(9.12 \pm 1.19) \times 10^{-6}$...	$\Delta\nu_{\text{WNM}}$ [GHz] . . .	-2.2 ± 1.3
χ^2/N_{dof} . . .	8.0/7	3.6/8	χ^2/N_{dof}	8.7/7

The parameters listed in this table are described in Eqs. 25, 26 and 27 where the dust SED is expressed in K_{RJ} units and normalized to 1 at 353 GHz. The fixed model parameters are $T_d = 18.7$ K, $\beta_{\text{d,FIR}}^I = 1.65$ (for model DI) and $\beta_{\text{d,mm}}^I = 1.52$ (for model DII).

the spectral index from 1.65 at FIR to 1.52 at microwave frequencies (Sect. 6) is accounted for by the BB component. The BB component accounts for about $(26 \pm 4)\%$ of the MBB component at 100 GHz and $(47 \pm 6)\%$ at 70 GHz, in agreement with what is reported by [Planck Collaboration Int. XVII \(2014\)](#) for the SED at high Galactic latitudes. The ratio between the BB and MBB components at a given frequency is constant at intermediate and high latitudes. The BB component could represent either magnetic dipole emission (MDE) from ferromagnetic particles, or inclusions in interstellar grains, as modelled by [Draine & Hensley \(2013\)](#).

MDE has been introduced by [Draine & Hensley \(2012\)](#) to explain the flattening of the dust SED at sub-mm wavelengths in the Small Magellanic Cloud ([Planck Collaboration XVII 2011](#)). The *Planck* data may indicate that this mechanism contributes to the microwave emission from our own Galaxy. The MDE interpretation is within the plausible range of models presented in [Draine & Hensley \(2013\)](#) for Galactic dust. If this is the correct interpretation, MDE from the Milky Way is detected here with a significance greater than 7σ (for a fixed spectral index of the MBB component).

Alternatively, the change in the dust spectral index from FIR to microwave frequencies in model DII, might indicate a change in the emission properties of the dust at long wavelengths ([Meny et al. 2007](#); [Paradis et al. 2011](#); [Jones et al. 2013](#)). There are two possible interpretations for this. First, the flattening could be due to a change in spectral index of the silicate grains. [Meny et al. \(2007\)](#) introduced a physical description of FIR/microwave dust emission, where the microwave dust opacity of amorphous grains is dominated by low energy transitions associated with disorder in the structure of the solids on atomic scales. This contribution is modelled by transitions in two-level systems (TLS). The TLS model is supported by experimental results on silicates ([Agladze et al. 1996](#); [Boudet et al. 2005](#); [Coupeaud et al. 2011](#)), which show that the opacity of amorphous silicate grains flattens towards long wavelengths. The TLS model has been used to model dust emission spectra by [Paradis et al. \(2011\)](#). The second interpretation is that the flattening of the dust SED could be due to an increasing contribution of carbon dust towards microwave frequencies. In the dust model of [Jones et al. \(2013\)](#), the emission from amorphous carbon grains becomes dominant at $\nu < 353$ GHz, and has a spectral index at microwave frequencies in agreement with that measured from the data.

We expect the polarization data to break the degeneracy between these three interpretations (MDE, TLS, and amorphous carbon) since they have different polarization signatures.

8. Dust spectral index for polarization

We now move to the analysis of the polarization data. Like in Sect. 6, we estimate the polarized dust spectral index ($\beta_{\text{d,mm}}^p$) at microwave frequencies ($\nu \leq 353$ GHz). We present the results of our data analysis and tests of its robustness against systematic effects.

8.1. Measuring $\beta_{\text{d,mm}}^p$

Using the polarization CC coefficients, $[\alpha_v^p]_{353}^{1T}$, we compute $R_{100}^p(353, 217)$ for each sky-patch using Eq. 18. Fig. 9 shows the values of $R_{100}^p(353, 217)$ versus the local dispersion of the polarized map at 353 GHz (σ_{353}^p) for all the sky-patches. To compute σ_{353}^p , we use a 1° smoothed map of P_{353} derived in [Planck Collaboration Int. XIX \(2014\)](#). We derive $\beta_{\text{d,mm}}^p$ for each sky-patch from $R_{100}^p(353, 217)$, taking into account the local estimate of T_d derived from $R^I(3000, 857)$ (Sect. 5.2). We assume that the temperature of the dust grains contributing to the polarization is the same as that determined for the dust emission in intensity. This is not necessarily true if the polarization is associated with specific dust grains, e.g., the silicates versus carbon dust ([Martin 2007](#); [Draine & Fraisse 2009](#)). This should be kept in mind in thinking of physical interpretations. Here we use the spectral indices $\beta_{\text{d,mm}}^p$ and $\beta_{\text{d,mm}}^I$ as a mathematical way to quantify the difference between the dust SED for intensity and polarization.

The scatter on the $R_{100}^p(353, 217)$ values increases sharply for $\sigma_{353}^p < 20 \mu\text{K}$. It is most likely the result of noise and systematic effects. The histogram of $\beta_{\text{d,mm}}^p$ from the 249 sky-patches with $\sigma_{353}^p > 20 \mu\text{K}$, is also presented in Fig. 9. The distribution of $\beta_{\text{d,mm}}^p$ has a mean value of 1.63, with a 1σ dispersion of 0.16. The statistical uncertainty on the mean $\beta_{\text{d,mm}}^p$ is computed from the 1σ dispersion divided by the square root of the number of independent sky-patches ($249/N_{\text{visit}}$) used, which is 0.02.

The mean value of the dust spectral index for polarization is different from that for intensity, 1.52 ± 0.02 (Sect. 6), but it is very close to the mean spectral index measured from the fit of the FIR dust SED at $\nu \geq 353$ GHz in [Planck Collaboration XI \(2014\)](#) over the same sky area. We have checked that our comparison of spectral indices in intensity and polarization is not biased by the selection of patches for polarization with $\sigma_{353}^p > 20 \mu\text{K}$. In the next section, we check whether the difference of spectral indices in intensity and polarization is a robust result against uncorrected systematics in the polarization data.

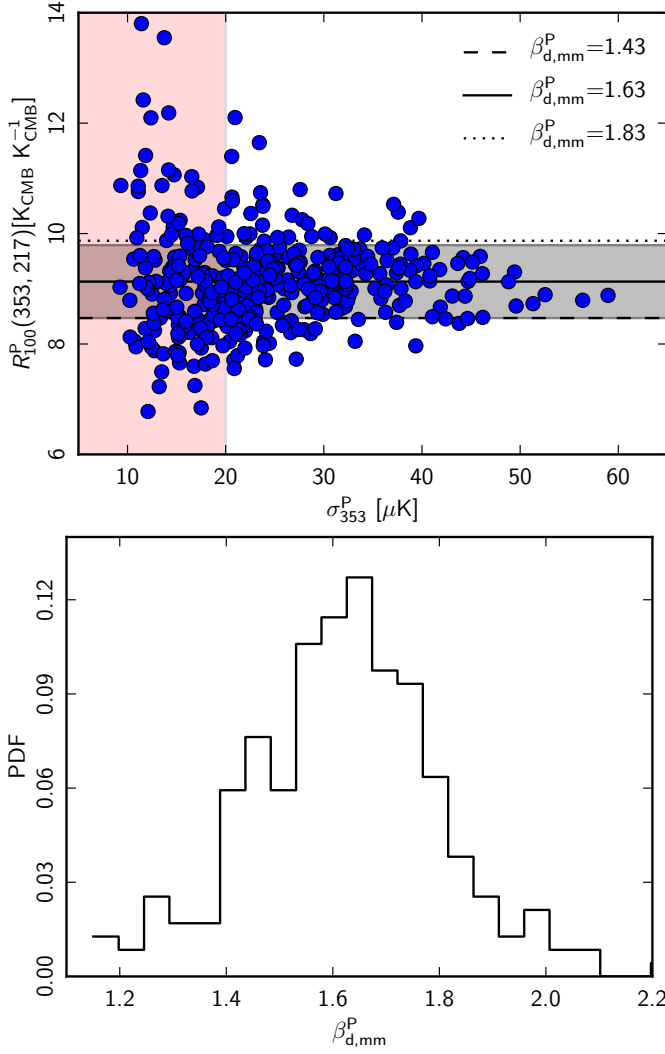


Fig. 9. *Top:* Colour ratio $R_{100}^P(353, 217)$ against the local dispersion of the polarization template at 353 GHz. The increase in the scatter of $R_{100}^P(353, 217)$ for $\sigma_{353}^P < 20 \mu\text{K}$ is likely due to systematic effects in the data. *Bottom:* Histogram of the $\beta_{d,mm}^P$ values inferred from $R_{100}^P(353, 217)$ for sky-patches with $\sigma_{353}^P > 20 \mu\text{K}$. The mean value of the spectral index for polarization is 1.63 ± 0.03 , which is different from that for intensity 1.52 ± 0.02 (Fig. 4).

8.2. Uncertainties in $\beta_{d,mm}^P$

To estimate the systematic uncertainty for the mean $\beta_{d,mm}^P$, we apply the CC analysis on the multiple *Planck* data sets, which include the combination of odd surveys (S1+S3) and even surveys (S2+S4), the full mission half-ring maps (HR1 and HR2), and the detector set maps (DS1 and DS2) (see Sect. 2.1.2 for more details). We use these subsets of the data as maps and templates at 353 GHz. Table 5 lists the derived mean $\beta_{d,mm}^P$ for the sky-patches with $\sigma_{353}^P > 20 \mu\text{K}$ from each combination of the data subsets. The combinations of maps we consider in Table 5 are unequally suited to estimate $\beta_{d,mm}^P$, because they involve systematics of different amplitude and degree of correlation between the three frequencies 100, 217 and 353 GHz used to compute $\beta_{d,mm}^P$. Table 5 lists the dispersion of the CC coefficients at 353 GHz, which we use as a measure of the uncertainty on

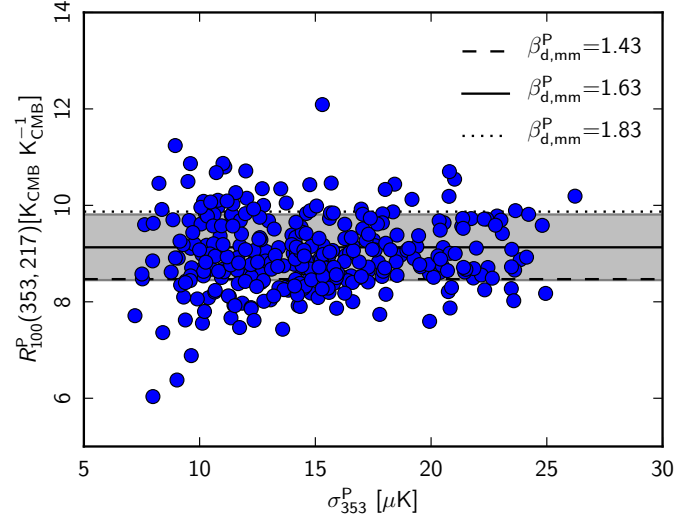


Fig. 10. Colour ratio $R_{100}^P(353, 217)$ obtained with filtered maps (Sect. 2.1.2) versus the local dispersion of the filtered polarization template at 353 GHz. The values are consistent with a mean value of $\beta_{d,mm}^P = 1.63$ (solid line, for the mean $T_d = 18.7 \text{ K}$), similar to that derived without filtering the maps.

Table 5. Polarized dust spectral indices derived using multiple subsets and templates of the *Planck* data.

Templates	Data sets	$\beta_{d,mm}^P$	$\sigma([\alpha_V^P]_{353}^{IT})^a$
.....	Full HR1	1.64	3.4×10^{-3}
Full DS1 and DS2	Full HR2	1.63	3.4×10^{-3}
.....	Survey 1+3	1.66	3.7×10^{-3}
.....	Survey 2+4	1.63	3.7×10^{-3}
.....	Full	1.55	12.0×10^{-3}
.....	Full HR1	1.56	12.0×10^{-3}
Surveys 1+3 and 2+4	Full HR2	1.55	12.0×10^{-3}
.....	Full DS1	1.53	12.1×10^{-3}
.....	Full DS2	1.57	12.1×10^{-3}
.....	Full	1.66	2.3×10^{-3}
.....	Full DS1	1.62	2.3×10^{-3}
Full HR1 and HR2	Full DS2	1.69	2.3×10^{-3}
.....	Surveys 1+3	1.69	2.5×10^{-3}
.....	Surveys 2+4	1.66	2.5×10^{-3}

^a $\sigma([\alpha_V^P]_{353}^{IT}) \equiv$ Dispersion of the CC coefficients at 353 GHz for each combination of templates and maps. We use this to weigh the values of $\beta_{d,mm}^P$.

$\beta_{d,mm}^P$ from systematic effects, because it measures the amplitude and degree of correlation of the data systematics between the two template maps at 353 GHz. The weighted dispersion of the $\beta_{d,mm}^P$ values in Table 5 is 0.02. This is our estimate of the 1σ uncertainty on the mean polarization spectra index from data systematic effects. Combining the systematic and statistical uncertainties, we find the mean polarized dust spectral index $\beta_{d,mm}^P = 1.63 \pm 0.02$ (syst.) ± 0.02 (stat.). The difference between the mean $\beta_{d,mm}^P$ and $\beta_{d,mm}^I$ has a 5σ significance if we consider only the statistical uncertainties. It is still a 3.5σ result if we also take into account our estimates of the systematic uncertainties on $\beta_{d,mm}^P$.

As a second test against systematic effects, we repeat the CC analysis with filtered *Planck* maps. The bandpass filter is described in Sect. 2.1.2 and it is used to filter the large scale systematic effects present in the *Planck* data (Planck Collaboration VI 2014). We cross-correlate the filtered Stokes Q and U maps of 353 GHz from the data sets, DS1 and DS2 with the filtered Stokes Q and U at a given frequency ν . Figure 10 presents the $R_{100}^P(353, 217)$ ratio as a function of the local dispersion of the 353 GHz polarized template, both computed on the filtered data. The mean $\beta_{d,mm}^P$ derived from the filtered data is consistent with the value obtained from the unfiltered maps and the dispersion of colour ratios is almost independent of the value of σ_{353}^P . This confirms our initial guess that the scatter on $R_{100}^P(353, 217)$ values at low σ_{353}^P in Fig. 9 is likely to be due to the systematic effects, which are the strongest at large angular scales (Planck Collaboration VI 2014).

9. Spectral energy distribution of dust polarization

We now derive the mean SED for the dust polarization and extend to polarization the parametric modelling already made on the dust SED in intensity (Sect. 7.2).

9.1. Mean polarized SED

Like in Sect. 7.1 for dust emission in intensity, the mean SED for polarization is obtained by averaging the polarization CC coefficients after CMB subtraction (see Sect. 5.3) over all sky-patches and is expressed in K_{RJ} units. The polarization SED is derived from the fit with one template, and is shown in Fig. 12. The polarization SED first decreases with decreasing frequency, then turns up below 60 GHz. This is the first time that such a behavior has been observed for polarized emission correlated with dust polarization, though it has been seen before for the total sky polarization (Bennett et al. 2013).

To estimate the uncertainties on the polarization SED, we repeat the CC analysis on subsets of the *WMAP* and *Planck* data, keeping the templates fixed to the polarized detector set maps (DS1 and DS2) at 353 GHz. For *WMAP*, we use the nine individual year polarized Stokes Q and U maps. For *Planck*, we use the subsets of data listed in Table 5, which include individual survey and half-ring maps. For each subset we compute the mean polarization SED for $\sigma_{353}^P > 20 \mu K$. The uncertainties on the polarized SED are computed in a similar manner to that discussed in Sect. 7. The mean polarized SED and associated uncertainties are listed in Table 6.

9.2. Low frequency rise of the polarization SED

In this section, we show that a synchrotron component correlated with dust is the most likely interpretation for the low frequency rise of the polarization SED.

9.2.1. Synchrotron polarization correlated with dust

The polarized dust and synchrotron emissions may be written as

$$[Q_\nu^s, U_\nu^s] = p_s I_\nu^s [\cos 2\psi_s, \sin 2\psi_s], \quad (28)$$

$$[Q_{353}^d, U_{353}^d] = p_d I_{353}^d [\cos 2\psi_d, \sin 2\psi_d], \quad (29)$$

where p_s and p_d are the polarization fractions, and ψ_s and ψ_d are the polarization angles, for synchrotron and dust, respectively.

After correlation with the 353 GHz I , Q and U templates, we have

$$\langle \alpha_\nu^P(s_{353}) \rangle \leq \frac{p_s}{p_d} \langle \alpha_\nu^I(s_{353}) \rangle, \quad (30)$$

where $\langle \alpha_\nu^I(s_{353}) \rangle$ and $\langle \alpha_\nu^P(s_{353}) \rangle$ are the mean SEDs of the synchrotron emission correlated with dust in intensity and polarization. The upper limit in Eq. 30 is obtained when the synchrotron and dust polarization angles are identical, which is not what is observed comparing the *Planck* 353 GHz and *WMAP* 23 GHz polarization data (Planck Collaboration Int. XIX 2014). Both emission processes trace the same large-scale Galactic magnetic field (GMF), but they give different weights to different parts of the line of sight. The CC analysis only keeps the synchrotron emission that arises from the same volume of interstellar space as the dust emission. For example, it is expected to filter out the synchrotron emission from the Galactic halo, where there is little dust. Thus, to validate our interpretation of the low frequency rise of the polarization SED with synchrotron and no AME polarization, we need to show that the upper limit in Eq. 30 holds.

The intrinsic polarization of synchrotron emission is about 75 % for typical relativistic electron spectra (Rybicki & Lightman 1979; Longair 1994), whereas the analysis of *Planck* polarization maps indicates that the intrinsic polarization of dust at 353 GHz can reach about 20 % (Planck Collaboration Int. XIX 2014; Planck Collaboration Int. XX 2014). To compute the synchrotron SED in intensity, $\langle \alpha_\nu^I(s_{353}) \rangle$, we combine the 353 GHz correlated CC coefficients, corrected for the CMB (Sect. 5.3), obtained from the fits with one and two templates (Sect. 4.2). The SED of the synchrotron emission correlated with dust is then obtained by taking the difference between the CC coefficients in Eqs. 8 and 11, and averaging over all sky-patches. It is shown in Fig. 11. Like in Sect. 7.1, the uncertainties are estimated using subsets of the *WMAP* and *Planck* data. We fit this synchrotron SED with a power-law (PL) model. The normalized amplitude of synchrotron emission at 23 GHz is $A_s^I = 0.29$. This is the ratio between the 23 and 353 GHz emission in units of K_{RJ} . The mean synchrotron spectral index derived from the fit is $\beta_s^I = -2.92 \pm 0.02$. The derived mean β_s^I of the dust-correlated synchrotron emission is consistent with the spectral index of 408-MHz-correlated synchrotron emission obtained using *WMAP* data (Miville-Deschênes et al. 2008; Dickinson et al. 2009; Gold et al. 2011; Ghosh et al. 2012).

Using $\langle \alpha_{23}^I(s_{353}) \rangle$, we find the theoretical upper limit on $\langle \alpha_{23}^P(s_{353}) \rangle$ to be

$$\langle \alpha_{23}^P(s_{353}) \rangle \leq \left(\frac{0.75}{0.20} \right) \times 0.29 = 1.1. \quad (31)$$

The measured value of $\langle [\tilde{\alpha}_{\nu,1353}^P]^T \rangle$ is 0.62 (shown in Fig. 12), which is within the upper limit. The difference between the measured and theoretical upper limit in Eq. 30 can be explained by the fact that polarization angles traced by synchrotron and dust emission are not perfectly aligned. We point out that this statement refers to the synchrotron emission correlated with the dust template in intensity, which is not one to one correlated with dust in polarization.

9.2.2. Upper limit on AME polarization

We can set an upper limit on the polarization fraction of AME by assuming that the synchrotron and dust polarization are totally uncorrelated. Within this hypothesis, the low frequency rise of the polarization SED is entirely due to polarized AME. Since

Table 6. Mean microwave SED for polarization computed using the CC analysis.

Quantity	Frequency [GHz]											
	Experiment											
	WMAP 23	Planck 28.4	WMAP 33	WMAP 41	Planck 44.1	WMAP 61	Planck 70.4	WMAP 94	Planck 100	Planck 143	Planck 217	Planck 353
$\langle [\tilde{\alpha}_\nu^P]_{353}^{1T} \rangle$	0.6197	0.3358	0.2439	0.1199	0.1368	0.0854	0.0844	0.1669	0.1717	0.2944	0.5531	1.0000
σ_{stat}	0.1140	0.0548	0.0391	0.0263	0.0236	0.0217	0.0143	0.0233	0.0078	0.0056	0.0072	0.0035
σ_{sys}	0.0155	0.0091	0.0137	0.0140	0.0074	0.0190	0.0090	0.0218	0.0012	0.0025	0.0016	0.0007
c_ν [%]	2.0	1.0	2.0	2.0	1.0	2.0	0.5	2.0	0.5	0.5	0.5	1.2
σ_{cmb}	0.0013	0.0006	0.0013	0.0013	0.0006	0.0012	0.0003	0.0011	0.0003	0.0002	0.0001	0.0000
σ_{tot}	0.1156	0.0556	0.0417	0.0299	0.0248	0.0289	0.0169	0.0321	0.0080	0.0063	0.0078	0.0101
S/N	5.4	6.0	5.8	4.0	5.5	3.0	5.0	5.2	21.6	46.7	70.5	99.3

$\langle [\tilde{\alpha}_\nu^P]_{353}^{1T} \rangle \equiv$ Mean polarization SED in K_{RJ} units, normalized to 1 at 353 GHz, from the correlation with the 353 GHz templates. The values are not colour corrected.

$\sigma_{\text{stat}} \equiv$ Statistical uncertainty on the mean polarization SED.

$\sigma_{\text{sys}} \equiv$ Systematic uncertainty on the mean polarization SED.

$c_\nu \equiv$ Uncertainties on the inter-calibration [%] between *Planck* and *WMAP* frequencies (Planck Collaboration I 2014; Bennett et al. 2013).

$\sigma_{\text{cmb}} \equiv$ Uncertainty on the mean polarized SED introduced by the CMB-subtraction multiplied by the inter-calibration factor c_ν .

$\sigma_{\text{tot}} \equiv$ Total uncertainty on the mean polarized SED.

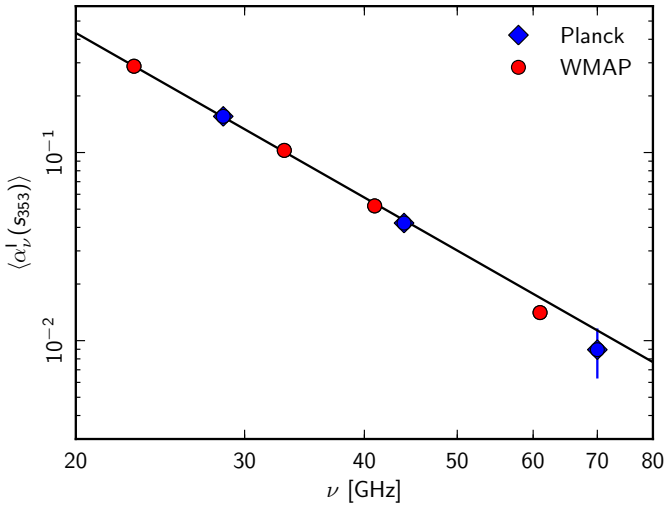


Fig. 11. Spectral energy distribution of the dust-correlated synchrotron emission in intensity. The SED is the ratio between the synchrotron emission at frequency ν and the dust emission at 353 GHz emission in units of K_{RJ} . The mean spectral index for the intensity is $\beta_s^I = -2.92 \pm 0.02$.

both AME and thermal dust emission are associated with interstellar matter, it is reasonable to assume that the polarization angles are the same for AME and dust. We obtain the 353 GHz correlated AME polarization at 23 GHz as,

$$\begin{aligned}
 \langle [\tilde{\alpha}_{23}^P]_{353}^{1T} \rangle &= \langle \alpha_{23}^P(a_{353}) \rangle = \frac{p_a}{p_d} \langle \alpha_{23}^I(a_{353}) \rangle, \\
 \text{i.e., } 0.62 &= \frac{p_a}{p_d} \langle \alpha_{23}^I(a_{353}) \rangle, \\
 \text{so } p_a &= \frac{p_d \times 0.62}{\langle \alpha_{23}^I(a_{353}) \rangle} \\
 &= \frac{p_d \times 0.62}{A_a^I}. \quad (32)
 \end{aligned}$$

We use the mean AME amplitude, $A_a^I = 1.18$, from model DII and Table 4, together with $p_d = 20\%$ (Planck Collaboration Int. XIX 2014; Planck Collaboration Int. XX 2014), to derive an upper limit on the intrinsic polarization fraction of AME of

about 10 %. This is much higher than upper limits reported from the analysis of compact sources (Dickinson et al. 2011; López-Caraballo et al. 2011; Rubiño-Martín et al. 2012) and theoretical predictions (Lazarian & Draine 2000; Hoang et al. 2013). Thus AME is unlikely to be the sole explanation for the low frequency rise of the polarization SED, even if we cannot exclude some contribution from AME.

9.3. Parametric modelling for polarized dust SED

In this section we present a spectral model that fits the observed polarization SED. We model the polarization SED with a combination of polarized synchrotron and dust components. This model does not include AME. We account for the rise of the SED towards the lowest frequencies with the synchrotron component. For the synchrotron component we use the PL model with two parameters: the amplitude; and the spectral index. The PL model of synchrotron emission is related to the power-law energy distribution of the cosmic-ray electron spectrum (Abdo et al. 2009; Ackermann et al. 2010, 2012). For the polarized dust, we use the model DI of the thermal dust emission in Sect. 7.2 with a constant (achromatic) polarization fraction p . The second model DII has a spectral index too low to match the polarization SED, within the assumption we make of a constant p for the MBB component. The model is the superposition of a power-law synchrotron spectrum (PSI), the MBB for the thermal dust emission, and the BB component (PDI). We refer to this model as PSI+PDI. It is described by the equation:

$$\begin{aligned}
 \langle [\tilde{\alpha}_\nu^P]_{353}^{1T} \rangle &= A_s^P \left(\frac{\nu}{23 \text{ GHz}} \right)^{\beta_s^P} + \left[A_d^P \left(\frac{\nu}{353 \text{ GHz}} \right)^{\beta_{d,\text{FIR}}^P} \right. \\
 &\quad \left. + A_b^P \left(\frac{\nu}{100 \text{ GHz}} \right)^{-2} \right] B_\nu(T_d), \quad (33)
 \end{aligned}$$

where A_s^P , A_d^P , and A_b^P are the amplitudes of polarized synchrotron, MBB, and BB components in K_{RJ} units, respectively. Like for the DI intensity model, we fix $\beta_{d,\text{FIR}}^P = 1.65$ and $T_d = 18.7 \text{ K}$. We fit four parameters: the synchrotron amplitude; the dust amplitude; the BB amplitude; and the synchrotron spectral index. We also fit this model with an additional constraint that the spectral index of 353 GHz correlated synchrotron component is the same for intensity and polarization. By doing so we

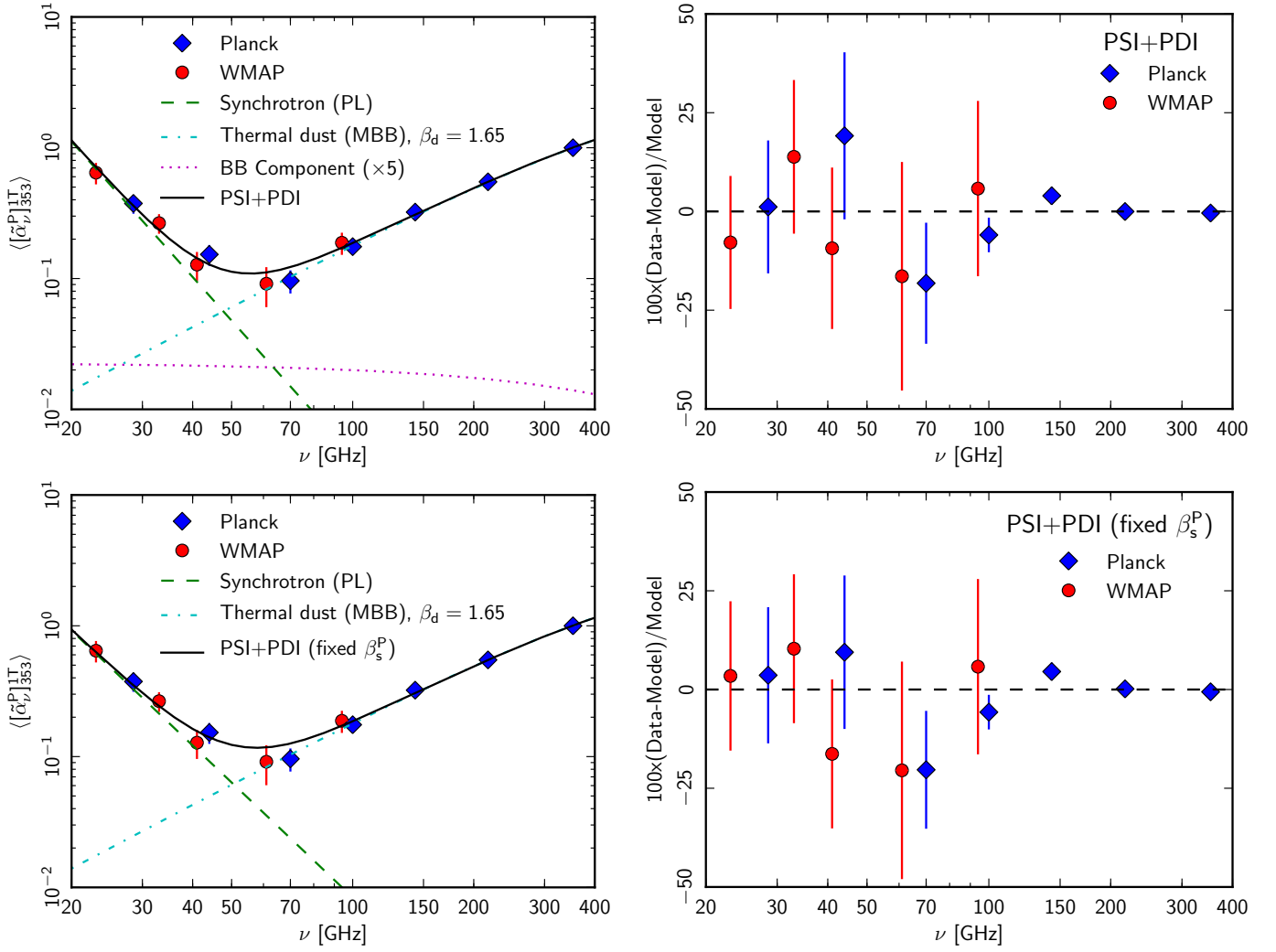


Fig. 12. Mean polarized SED normalized at 353 GHz correlated with the Stokes Q and U 353 GHz maps. The polarized spectral model with and without the constraint on β_s^P match the observed data points. The amplitude of the BB component is scaled up by a factor of five to appear in the top plot.

have one less parameter to fit and increase the number of degrees of freedom by one.

The fits to the polarization SED for model with and without the constraint on β_s^P are shown in Fig. 12. The parameters for the best-fit models are listed in Table 7. The two models provide very similar fits to the observed polarized SED, with the contribution of the BB component consistent with zero within the uncertainties. If we force the spectral indices of the synchrotron for intensity and polarization to be equal, we find a good fit to the polarization SED. These results are further discussed in the next section.

10. Comparison of the dust SEDs for intensity and polarization

We now compare the dust SEDs for intensity and polarization and discuss the frequency dependence of the polarization fraction within the context of existing dust models.

Table 7. Results of the spectral fits to the mean polarized dust SED obtained using *Planck* and *WMAP* data.

Parameters ^a	Unconstrained β_s^P	Fixed β_s^P
$A_d^P \dots \dots \dots$	$(22.76 \pm 0.29) \times 10^{-6}$	$(22.88 \pm 0.27) \times 10^{-6}$
$A_s^P \dots \dots \dots$	0.69 ± 0.10	0.62 ± 0.07
$\beta_s^P \dots \dots \dots$	-3.44 ± 0.51	-2.92
$A_b^P \dots \dots \dots$	$(0.79 \pm 1.59) \times 10^{-6}$	$(-0.29 \pm 1.36) \times 10^{-6}$
$\chi^2/N_{\text{dof}} \dots$	10.3/8	11.7/9

^a The parameters of the model PSI+PDI are described in Eq. 33 for fixed $T_d = 18.7$ K and $\beta_{d,\text{FIR}}^P = 1.65$.

10.1. Spectral dependence of the polarization fraction

The dust SED for intensity after AME subtraction is shown in the top panel of Fig. 13, between 70 and 353 GHz. The subtraction of the three different AME models yields the same dust SED at $\nu > 70$ GHz. From the top panel of Fig. 13, it is clearly evident that the flattening of the dust SED can be accounted for equally

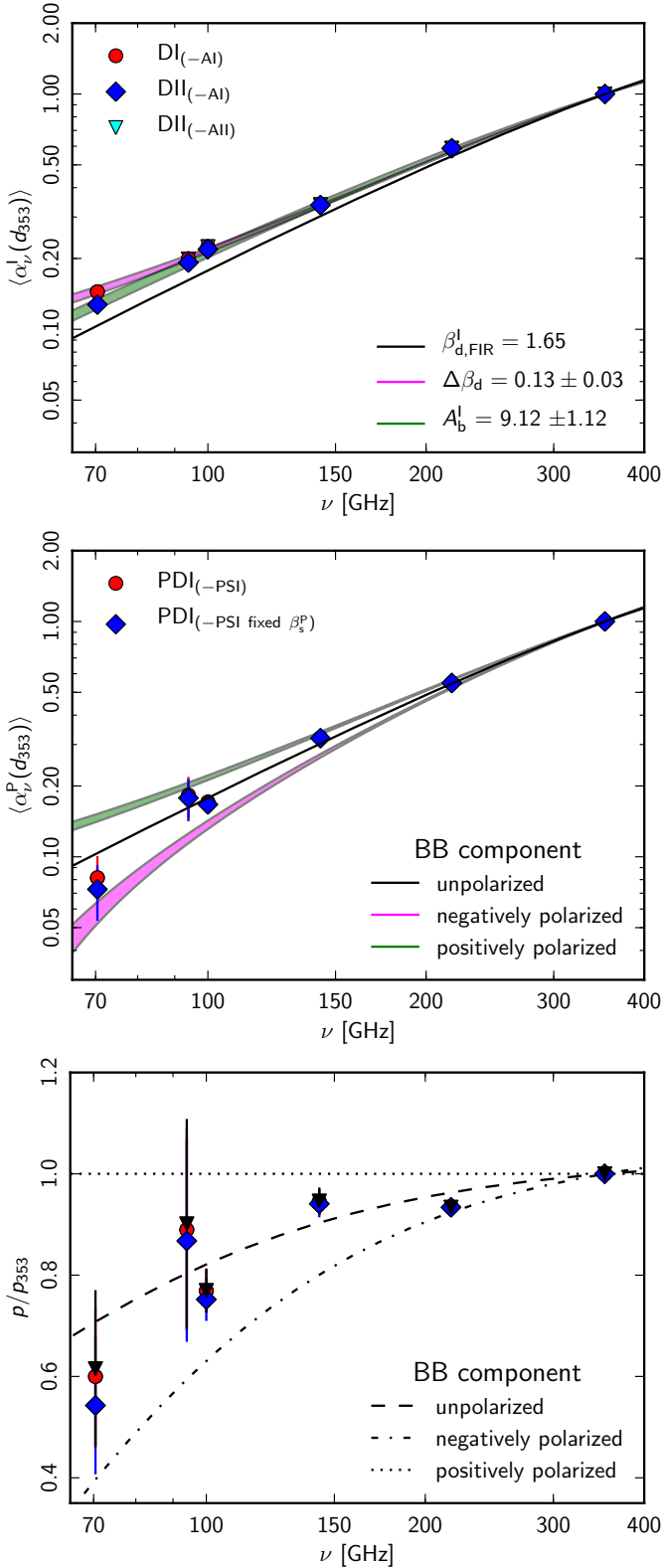


Fig. 13. Frequency dependence of the dust SED in intensity without AME (*top*), in polarization without synchrotron (*middle*), and the polarization fraction (*bottom*) for the different dust models. The SEDs are plotted in units of K_{RJ} and normalized to 1 at 353 GHz. We used the same sky-patches ($\sigma_{353}^P > 20 \mu K$) for both the intensity and polarization analysis.

well by changing the dust spectral index ($\Delta\beta_d$) or by the BB component.

The dust SED for polarization is shown in the middle panel of Fig. 13 after subtraction of the two best-fit synchrotron models. The significant difference between the two spectral indices (0.5, see Table 7) for the polarized synchrotron emission has a very small impact on the dust polarization SED even at 70 GHz. This shows that our dust polarization SED is robust with respect to uncertainties on the spectral index of polarized synchrotron, including a possible steepening of the spectrum with increasing frequencies as discussed in Gold et al. (2011). The polarization fraction, shown in the bottom panel of Fig. 13, is normalized with respect to the data point at 353 GHz. The uncertainties on p include the uncertainties from both P and I .

In the middle and bottom panels, we plot three curves that correspond to schematic assumptions about the polarization of the BB component. The middle curve assumes that the BB component is unpolarized, while for the top and bottom curves the BB component has the same degree of polarization as the MBB component, with positive and negative signs, respectively. The dotted line in the bottom panel represents a positive polarization of the BB component, equal to that of the MBB component. Schematically, this is what is expected if the spectral flattening of the dust SED in intensity comes from interstellar silicates within the TLS model (Sect. 7.3). The dashed line corresponds to no polarization of the BB component. This is expected if the flattening of the dust SED in intensity is due to carbon dust and if the carbon grains are not aligned (Martin 2007). The dot-dashed line corresponds to a polarization of the BB component, which is orthogonal to that of the MBB component. This is the qualitative expectation for MDE coming from magnetic inclusions (Draine & Hensley 2013). In the next sections, we further discuss these three interpretations.

10.2. The contribution of carbon dust and silicates to polarization

The flattening of the dust SED in intensity and the difference between the intensity and the polarization SEDs may come from the different polarization properties of silicate and carbon grains (Hildebrand et al. 1999; Martin 2007). We address this interpretation using the models from Draine & Li (2007), Compiègne et al. (2011), and Jones et al. (2013).

In these three models, the thermal dust emission is the electric dipole emission from two types of grains, silicates and carbon grains, with distinct optical properties and thereby temperatures. The first two models use the same optical properties for silicates, but distinct properties for carbon grains; Draine & Li (2007) use the optical properties of graphite, while Compiègne et al. (2011) use results from laboratory measurements of amorphous carbon. The spectral index for carbon grains is 2 in the Draine & Li (2007) model and 1.6 in Compiègne et al. (2011). Over microwave frequencies, the opacity of silicates scales as $\nu^{1.6}$ in both models. Jones et al. (2013) use optical properties of amorphous carbon grains, which depend on the hydrogen fraction and degree of aromatization (Jones 2012). The spectral index of the carbon dust at 353 GHz varies between 1.2 and 2.3, depending on the nature of the carbon grains (see figure 14 of Jones et al. 2013 for more details).

SEDs from the first two models have been compared to the Planck dust SED in intensity in Planck Collaboration Int. XVII (2014). The differences between the model and the data are within 5–15 % at $\nu < 353$ GHz. Draine & Fraisse (2009) have used the Draine & Li (2007) dust model to compute spectra for dust polarization. They predict a systematic increase of the polarization fraction p in microwave frequencies when only sili-

cates contribute to dust polarization. This prediction is the opposite to what we observe. However, model predictions for the spectral dependency of p are related to the difference in spectral index between carbon and silicate grains, which is not known. Thus, a difference between carbon and silicate polarization may be the correct physical interpretation of the spectral dependence of p , even if the data do not match the [Draine & Fraisse \(2009\)](#) model. Calculations of the polarized SED for the [Compiègne et al. \(2011\)](#) and [Jones et al. \(2013\)](#) models are needed to assess quantitatively this interpretation. In the [Compiègne et al. \(2011\)](#) model, the spectra from silicates and carbon grains are very similar at long wavelengths and we do not expect p to depend on wavelength when only silicates contribute to the polarization. In the [Jones et al. \(2013\)](#) model the contribution from carbon dust grains could be dominant at $\nu < 353$ GHz. We refer to the companion *Planck* paper [Planck Collaboration Int. XXI \(2014\)](#) for a comparison of the [Draine & Fraisse \(2009\)](#) model with the measured ratios of polarization between 353 GHz and the optical.

10.3. Magnetic dipole emission

The dust SED in polarization allows us to discuss two possible interpretations, TLS and MDE (Sect. 7.3), of the decrease of the spectral index of the thermal dust emission in intensity, from FIR to microwave frequencies, found in this work, as well as the diffuse emission in the Galactic plane in [Planck Collaboration Int. XIV \(2014\)](#) and at high Galactic latitudes in [Planck Collaboration Int. XVII \(2014\)](#).

Within the TLS model, the flattening of the dust SED in intensity would be due to a decrease of the spectral index of silicate grains at long wavelengths. Since silicate grains are polarized, the flattening of the dust SED should also be seen in polarization. This expectation is not supported by the results of our data analysis, namely the difference in spectral indices of the thermal dust emission in intensity and polarization ($\beta_{\text{d,mm}}^I$ and $\beta_{\text{d,mm}}^P$) reported in Sect. 8.2.

For MDE, if the magnetic particles are inclusions randomly-oriented within interstellar grains, their emission is polarized in a direction perpendicular to that of the dipolar electric emission ([Draine & Hensley 2013](#)). In this case, we expect the BB component to reduce the polarization of the MBB component. This means that the amplitude of the polarized contribution of the BB component to the fit (model PSI+PDI) of the polarized SED should be negative in Fig. 13. A fit of the SEDs in polarization and intensity with the model of [Draine & Hensley \(2013\)](#) would be necessary to assess this interpretation quantitatively.

11. Conclusion

We have characterized the frequency dependence of dust emission in intensity and polarization by analysing *Planck* data over 39 % of the sky at intermediate Galactic latitudes. We use the *Planck* 353 GHz I , Q , and U maps as templates for dust emission in intensity and polarization. We cross-correlate them with the *Planck* and *WMAP* data, at 12 frequencies from 23 to 353 GHz. The main results of the data analysis are as follows.

- The mean spectral index of the dust emission measured between 100 and 353 GHz is $\beta_{\text{d,mm}}^I = 1.52 \pm 0.02$. This value agrees with that reported by [Planck Collaboration Int. XVII \(2014\)](#) for the high Galactic latitude sky and [Planck Collaboration Int. XIV \(2014\)](#) for diffuse emission in the Galactic plane. The microwave spectral index $\beta_{\text{d,mm}}^I$ is

smaller than that at far-infrared wavelengths derived from fits to the *Planck* data at $\nu \geq 353$ GHz in [Planck Collaboration Int. XVII \(2014\)](#) and [Planck Collaboration XI \(2014\)](#).

- We determine the mean dust SED in intensity from 23 to 353 GHz. We separate the dust and AME contributions to the SED. The dust contribution is well fit by combining the modified blackbody spectrum with a spectral index of 1.65 and a blackbody component, both at the same mean temperature of 18.7 K. The blackbody component accounts for $(26 \pm 4) \%$ of the dust emission at 100 GHz, a value in agreement with that reported by [Planck Collaboration Int. XVII \(2014\)](#) for the dust SED at high Galactic latitudes. This could represent magnetic dipole emission from Galactic dust, as modelled by [Draine & Hensley \(2013\)](#). Alternatively, it could represent the contribution from low energy transitions in amorphous solids to the opacity of interstellar dust within the TLS model ([Meny et al. 2007](#)), or flattening of the dust SED due to carbonaceous dust as suggested by [Jones et al. \(2013\)](#).
- The mean spectral index for dust polarization measured between 100 and 353 GHz is $\beta_{\text{d,mm}}^P = 1.63 \pm 0.03$, assuming the temperature of aligned dust grains contributing to the polarization is the same as that determined from the dust in intensity. We show that the difference with the spectral index measured in a similar way for dust intensity is a robust result against known systematic effects.
- We determine the SED of the dust-correlated polarized emission from 23 to 353 GHz. This SED decreases with decreasing frequency and turns up below 60 GHz, very much like the dust SED in intensity due to AME. We show that the low frequency rise of the polarization SED may be explained by synchrotron polarization correlated with dust, and that it does not imply that AME is polarized.
- We use a parametric model to separate the synchrotron and dust polarization and to characterize the spectral dependence of the dust polarization fraction. The polarization fraction p of the dust emission decreases by $(34 \pm 10) \%$ from 353 to 70 GHz. We discuss this result within the context of existing dust models. It could indicate differences in polarization efficiency among components of interstellar dust (e.g., carbon and silicate grains). Alternatively, it could be a signature of magnetic dipole emission from ferromagnetic inclusions within interstellar grains. These two possible interpretations must be tested quantitatively comparing the data with dust models.

Our observational results provide inputs to quantify and optimize the separation between Galactic and CMB polarization. Our CC analysis yields a spectral decomposition of the diffuse emission into its main components: thermal emission from dust; free-free; synchrotron; and AME. This spectral decomposition may be combined with power spectra of the templates, as discussed in Appendix D, to quantify the Galactic emission in intensity as a function of the observed frequency and multipole (see Figs. 27 and 28 in [Planck Collaboration I \(2014\)](#)). For polarization, we are currently missing a synchrotron polarization template that is free from Faraday rotation. Polarized synchrotron templates, which are expected from C-BASS ([King et al. 2010](#)) at 5 GHz and QUIJOTE ([Hoyland et al. 2012](#)) between 10 and 20 GHz, will be important for future correlation analyses.

Acknowledgements. The *Planck* Collaboration acknowledges the support of: ESA; CNES and CNRS/INSU-IN2P3-INP (France); ASI, CNR, and INAF (Italy); NASA and DoE (USA); STFC and UKSA (UK); CSIC, MICINN and JA (Spain); Tekes, AoF and CSC (Finland); DLR and MPG (Germany); CSA (Canada); DTU Space (Denmark); SER/SSO (Switzerland); RCN

(Norway); SFI (Ireland); FCT/MCTES (Portugal); and DEISA (EU). A detailed description of the *Planck* Collaboration and a list of its members can be found at http://www.rssd.esa.int/index.php?project=PLANCK&page=Planck_Collaboration. The research leading to these results has received funding from the European Research Council under the European Union's Seventh Framework Programme (FP7/2007-2013) / ERC grant agreement n 267934. We acknowledge the use of the Legacy Archive for Microwave Background Data Analysis (LAMBDA), part of the High Energy Astrophysics Science Archive Center (HEASARC). HEASARC/LAMBDA is a service of the Astrophysics Science Division at the NASA Goddard Space Flight Center. Some of the results in this paper have been derived using the HEALPix package.

References

- Abdo, A. A., Ackermann, M., Ajello, M., et al. 2009, *Physical Review Letters*, 102, 181101
- Ackermann, M., Ajello, M., Allafort, A., et al. 2012, *Physical Review Letters*, 108, 011103
- Ackermann, M., Ajello, M., Atwood, W. B., et al. 2010, *Phys. Rev. D*, 82, 092004
- Agladze, N. I., Sievers, A. J., Jones, S. A., Burlitch, J. M., & Beckwith, S. V. W. 1996, *ApJ*, 462, 1026
- Ali-Haïmoud, Y., Hirata, C. M., & Dickinson, C. 2009, *MNRAS*, 395, 1055
- Banday, A. J., Dickinson, C., Davies, R. D., Davis, R. J., & Górski, K. M. 2003, *MNRAS*, 345, 897
- Banday, A. J., Gorski, K. M., Bennett, C. L., et al. 1996, *ApJ*, 468, L85
- Bennett, C. L., Larson, D., Weiland, J. L., et al. 2013, *ApJS*, 208, 20
- Bonaldi, A., Ricciardi, S., Leach, S., et al. 2007, *MNRAS*, 382, 1791
- Boudet, N., Mutschke, H., Nayral, C., et al. 2005, *ApJ*, 633, 272
- Brandt, T. D. & Draine, B. T. 2012, *ApJ*, 744, 129
- Chiar, J. E., Adamson, A. J., Whittet, D. C. B., et al. 2006, *ApJ*, 651, 268
- Chon, G., Challinor, A., Prunet, S., Hivon, E., & Szapudi, I. 2004, *MNRAS*, 350, 914
- Compiègne, M., Verstraete, L., Jones, A., et al. 2011, *A&A*, 525, A103
- Coupeaud, A., Demyk, K., Meny, C., et al. 2011, *A&A*, 535, A124
- Davies, R. D., Dickinson, C., Banday, A. J., et al. 2006, *MNRAS*, 370, 1125
- de Oliveira-Costa, A., Tegmark, M., Gutierrez, C. M., et al. 1999, *ApJ*, 527, L9
- Dickinson, C., Davies, R. D., & Davis, R. J. 2003, *MNRAS*, 341, 369
- Dickinson, C., Eriksen, H. K., Banday, A. J., et al. 2009, *ApJ*, 705, 1607
- Dickinson, C., Peel, M., & Vidal, M. 2011, *MNRAS*, 418, L35
- Dobler, G. & Finkbeiner, D. P. 2008, *ApJ*, 680, 1222
- Draine, B. T. & Fraisse, A. A. 2009, *ApJ*, 696, 1
- Draine, B. T. & Hensley, B. 2012, *ApJ*, 757, 103
- Draine, B. T. & Hensley, B. 2013, *ApJ*, 765, 159
- Draine, B. T. & Lazarian, A. 1998, *ApJ*, 508, 157
- Draine, B. T. & Lazarian, A. 1999, in *Bulletin of the American Astronomical Society*, Vol. 31, American Astronomical Society Meeting Abstracts #194, 890
- Draine, B. T. & Li, A. 2007, *ApJ*, 657, 810
- Erickson, W. C. 1957, *ApJ*, 126, 480
- Finkbeiner, D. P., Davis, M., & Schlegel, D. J. 1999, *ApJ*, 524, 867
- Gardner, F. F. & Whiteoak, J. B. 1966, *ARA&A*, 4, 245
- Ghosh, T., Banday, A. J., Jaffe, T., et al. 2012, *MNRAS*, 422, 3617
- Gold, B., Odegard, N., Weiland, J. L., et al. 2011, *ApJS*, 192, 15
- Gorski, K. M., Banday, A. J., Bennett, C. L., et al. 1996, *ApJ*, 464, L11
- Górski, K. M., Hivon, E., Banday, A. J., et al. 2005, *ApJ*, 622, 759
- Haslam, C. G. T., Salter, C. J., Stoffel, H., & Wilson, W. E. 1982, *A&AS*, 47, 1
- Hauser, M. G., Arendt, R. G., Kelsall, T., et al. 1998, *ApJ*, 508, 25
- Hildebrand, R. H., Dotson, J. L., Dowell, C. D., Schleuning, D. A., & Vaillancourt, J. E. 1999, *ApJ*, 516, 834
- Hoang, T., Lazarian, A., & Draine, B. T. 2011, *ApJ*, 741, 87
- Hoang, T., Lazarian, A., & Martin, P. G. 2013, *ArXiv e-prints*
- Hoyland, R. J., Aguiar-González, M., Aja, B., et al. 2012, in *Society of Photo-Optical Instrumentation Engineers (SPIE) Conference Series*, Vol. 8452, Society of Photo-Optical Instrumentation Engineers (SPIE) Conference Series
- Jones, A. P. 2012, *A&A*, 542, A98
- Jones, A. P., Fanciullo, L., Köhler, M., et al. 2013, *A&A*, 558, A62
- Kalberla, P. M. W., Burton, W. B., Hartmann, D., et al. 2005, *A&A*, 440, 775
- King, O. G., Copley, C., Davies, R., et al. 2010, in *Society of Photo-Optical Instrumentation Engineers (SPIE) Conference Series*, Vol. 7741, Society of Photo-Optical Instrumentation Engineers (SPIE) Conference Series
- Kogut, A., Banday, A. J., Bennett, C. L., et al. 1996, *ApJ*, 464, L5
- Kogut, A., Dunkley, J., Bennett, C. L., et al. 2007, *ApJ*, 665, 355
- Lagache, G. 2003, *A&A*, 405, 813
- Lazarian, A. & Draine, B. T. 2000, *ApJ*, 536, L15
- Lehtinen, K., Juvela, M., & Mattila, K. 2010, *A&A*, 517, A79
- Leitch, E. M., Readhead, A. C. S., Pearson, T. J., & Myers, S. T. 1997, *ApJ*, 486, L23
- Longair, M. S. 1994, *High energy astrophysics. Volume 2. Stars, the Galaxy and the interstellar medium.* (Cambridge University Press)
- López-Caraballo, C. H., Rubiño-Martín, J. A., Rebolo, R., & Génova-Santos, R. 2011, *ApJ*, 729, 25
- Macellari, N., Pierpaoli, E., Dickinson, C., & Vaillancourt, J. E. 2011, *MNRAS*, 418, 888
- Marinucci, D., Pietrobon, D., Balbi, A., et al. 2008, *MNRAS*, 383, 539
- Martin, P. G. 2007, in *EAS Publications Series*, Vol. 23, EAS Publications Series, ed. M.-A. Miville-Deschênes & F. Boulanger, 165–188
- Mennella, A., Butler, R. C., Curto, A., et al. 2011, *A&A*, 536, A3
- Meny, C., Gromov, V., Boudet, N., et al. 2007, *A&A*, 468, 171
- Miville-Deschênes, M.-A., Ysard, N., Lavabre, A., et al. 2008, *A&A*, 490, 1093
- Page, L., Hinshaw, G., Komatsu, E., et al. 2007, *ApJS*, 170, 335
- Paradis, D., Bernard, J.-P., Mény, C., & Gromov, V. 2011, *A&A*, 534, A118
- Planck HFI Core Team. 2011, *A&A*, 536, A4
- Planck Collaboration I. 2011, *A&A*, 536, A1
- Planck Collaboration XVII. 2011, *A&A*, 536, A17
- Planck Collaboration XX. 2011, *A&A*, 536, A20
- Planck Collaboration XXIV. 2011, *A&A*, 536, A24
- Planck Collaboration XXV. 2011, *A&A*, 536, A25
- Planck Collaboration I. 2014, *A&A*, in press, [arXiv:astro-ph/1303.5062]
- Planck Collaboration II. 2014, *A&A*, in press, [arXiv:astro-ph/1303.5063]
- Planck Collaboration III. 2014, *A&A*, in press, [arXiv:astro-ph/1303.5064]
- Planck Collaboration IV. 2014, *A&A*, in press, [arXiv:astro-ph/1303.5065]
- Planck Collaboration VI. 2014, *A&A*, in press, [arXiv:astro-ph/1303.5067]
- Planck Collaboration VII. 2014, *A&A*, in press, [arXiv:astro-ph/1303.5068]
- Planck Collaboration VIII. 2014, *A&A*, in press, [arXiv:astro-ph/1303.5069]
- Planck Collaboration IX. 2014, *A&A*, in press, [arXiv:astro-ph/1303.5070]
- Planck Collaboration X. 2014, *A&A*, in press, [arXiv:astro-ph/1303.5071]
- Planck Collaboration XI. 2014, *A&A*, in press, [arXiv:astro-ph/1312.1300]
- Planck Collaboration XII. 2014, *A&A*, in press, [arXiv:astro-ph/1303.5072]
- Planck Collaboration XIII. 2014, *A&A*, in press, [arXiv:astro-ph/1303.5073]
- Planck Collaboration XIV. 2014, *A&A*, in press, [arXiv:astro-ph/1303.5074]
- Planck Collaboration XV. 2014, *A&A*, in press, [arXiv:astro-ph/1303.5075]
- Planck Collaboration XVI. 2014, *A&A*, in press, [arXiv:astro-ph/1303.5076]
- Planck Collaboration XXX. 2014, *A&A*, in press, [arXiv:astro-ph/1309.0382]
- Planck Collaboration Int. IX. 2013, *A&A*, 554, A139
- Planck Collaboration Int. XII. 2013, *A&A*, 557, A53
- Planck Collaboration Int. XIV. 2014, *A&A*, in press, [arXiv:astro-ph/1307.6815]
- Planck Collaboration Int. XV. 2014, *A&A*, in press, [arXiv:astro-ph/1309.1357]
- Planck Collaboration Int. XVII. 2014, *A&A*, in press, [arXiv:astro-ph/1312.5446]
- Planck Collaboration Int. XIX. 2014, *A&A*, submitted, [arXiv:astro-ph/1405.0871]
- Planck Collaboration Int. XX. 2014, *A&A*, submitted, [arXiv:astro-ph/1405.0872]
- Planck Collaboration Int. XXI. 2014, *A&A*, submitted, [arXiv:astro-ph/1405.0873]
- Reach, W. T., Wall, W. F., & Odegard, N. 1998, *ApJ*, 507, 507
- Rubiño-Martín, J. A., López-Caraballo, C. H., Génova-Santos, R., & Rebolo, R. 2012, *Advances in Astronomy*, 2012
- Rybicki, G. B. & Lightman, A. P. 1979, *Radiative processes in astrophysics* (Wiley-Interscience)
- Seon, K.-I. & Witt, A. N. 2012, *ApJ*, 758, 109
- Silsbee, K., Ali-Haïmoud, Y., & Hirata, C. M. 2011, *MNRAS*, 411, 2750
- Smith, C. H., Wright, C. M., Aitken, D. K., Roche, P. F., & Hough, J. H. 2000, *MNRAS*, 312, 327
- Tauber, J. A., Mandolesi, N., Puget, J.-L., et al. 2010, *A&A*, 520, A1
- Vaillancourt, J. E. 2002, *ApJS*, 142, 53
- Vaillancourt, J. E., Dowell, C. D., Hildebrand, R. H., et al. 2008, *ApJ*, 679, L25
- Vaillancourt, J. E. & Matthews, B. C. 2012, *ApJS*, 201, 13
- Witt, A. N., Gold, B., Barnes, III, F. S., et al. 2010, *ApJ*, 724, 1551
- Wolff, M. J., Clayton, G. C., Kim, S.-H., Martin, P. G., & Anderson, C. M. 1997, *ApJ*, 478, 395
- Ysard, N., Miville-Deschênes, M. A., & Verstraete, L. 2010, *A&A*, 509, L1

Appendix A: Derivation of the CC coefficients

This appendix details how we compute the dust SED using the CC analysis in Sect. 4.2. For simplicity, we present the simplest case for intensity from the fit with one template.

We minimize the χ^2_I between the data and the 353 GHz template maps, as expressed in Eq. 7. The CC coefficient is then

given as

$$[\alpha_{\nu}^I]_{353}^{1T} = \frac{\sum_{k=1}^{N_{\text{pix}}} \hat{I}_{\nu}(k) \cdot \hat{I}_{353}(k)}{\sum_{k=1}^{N_{\text{pix}}} \hat{I}_{353}(k)^2}, \quad (\text{A.1})$$

where \hat{I}_{ν} and \hat{I}_{353} are the data and 353 GHz template with mean values (computed over the N_{pix}) subtracted. The observed *Planck* map at a given frequency is written as the sum of the CMB signal, the Galactic signals (synchrotron, free-free, dust and AME) and noise as

$$I_{\nu}(k) = I^c(k) + I_{\nu}^d(k) + I_{\nu}^s(k) + I_{\nu}^f(k) + I_{\nu}^a(k) + I_{\nu}^n(k), \quad (\text{A.2})$$

where the superscripts c, d, s, f, a, and n represent the CMB, dust, synchrotron, free-free, AME, and noise, respectively. Combining Eqs. A.1 and A.2 we find

$$\begin{aligned} [\alpha_{\nu}^I]_{353}^{1T} &= N \sum_{k=1}^{N_{\text{pix}}} [\hat{I}^c(k) + \hat{I}_{\nu}^d(k) + \hat{I}_{\nu}^s(k) + \hat{I}_{\nu}^f(k) + \hat{I}_{\nu}^a(k) + \hat{I}_{\nu}^n(k)] \\ &\times [\hat{I}^c(k) + \hat{I}_{353}^d(k) + \hat{I}_{353}^s(k) + \hat{I}_{353}^f(k) + \hat{I}_{353}^a(k) + \hat{I}_{353}^n(k)], \end{aligned} \quad (\text{A.3})$$

where $N = (1 / \sum_{k=1}^{N_{\text{pix}}} \hat{I}_{353}(k)^2)$ is the normalization factor. At HFI frequencies, we can neglect the contribution of the synchrotron, free-free, AME, and noise within our global mask. This reduces Eq. A.3 to

$$\begin{aligned} [\alpha_{\nu}^I]_{353}^{1T} &= N \sum_{k=1}^{N_{\text{pix}}} (\hat{I}^c(k) + \hat{I}_{\nu}^d(k)) \times (\hat{I}^c(k) + \hat{I}_{353}^d(k)) \\ &= N \sum_{k=1}^{N_{\text{pix}}} [\hat{I}^c(k) (\hat{I}^c(k) + \hat{I}_{353}^d(k)) + \hat{I}_{\nu}^d(k) (\hat{I}^c(k) + \hat{I}_{353}^d(k))] \\ &= \alpha(c_{353}) + N \sum_{k=1}^{N_{\text{pix}}} \hat{I}_{\nu}^d(k) (\hat{I}^c(k) + \hat{I}_{353}^d(k)). \end{aligned} \quad (\text{A.4})$$

The CMB contribution, $\alpha(c_{353})$, is the CC coefficient obtained by correlating the CMB signal map with the 353 GHz template, which is independent of frequency. The dust emission at a given frequency is a scaled version of 353 GHz dust emission, $\hat{I}_{\nu}^d(k) = \alpha_{\nu}^d \hat{I}_{353}^d(k)$, where α_{ν}^d is the mean dust SED over the given sky-patch. The CC coefficient is then

$$\begin{aligned} [\alpha_{\nu}^I]_{353}^{1T} &= \alpha(c_{353}) + \alpha_{\nu}^d N \sum_{k=1}^{N_{\text{pix}}} \hat{I}_{353}^d(k) (\hat{I}^c(k) + \hat{I}_{353}^d(k)) \\ &= \alpha(c_{353}) + \alpha_{\nu}^I(d_{353}). \end{aligned} \quad (\text{A.5})$$

where $\alpha_{\nu}^I(d_{353})$ is proportional to the mean dust SED. The colour ratio $R_{100}^I(353, 217)$ is then given by

$$\begin{aligned} R_{100}^I(353, 217) &= \frac{[\alpha_{353}^I]_{353}^{1T} - [\alpha_{100}^I]_{353}^{1T}}{[\alpha_{217}^I]_{353}^{1T} - [\alpha_{100}^I]_{353}^{1T}} \\ &= \frac{\alpha_{353}^d - \alpha_{100}^d}{\alpha_{217}^d - \alpha_{100}^d}. \end{aligned} \quad (\text{A.6})$$

In the ratio the scaling between the $\alpha_{\nu}^I(d_{353})$ and α_{ν}^d goes away. The colour ratio only depends on the dust spectral properties and not on the CMB signal. The extension of Eq. A.5 in the presence of AME, synchrotron, and free-free emission at the *WMAP* and LFI frequencies is given by Eq. 8.

The CMB contribution, $\alpha(c_{353})$, in the presence of inverse noise-weighting can be written as

$$\alpha(c_{353}) = \frac{\sum_{k=1}^{N_{\text{pix}}} w_{\nu}(k) \hat{I}^c(k) (\hat{I}^c(k) + \hat{I}_{353}^d(k))}{\sum_{k=1}^{N_{\text{pix}}} w_{\nu}(k) \hat{I}_{353}(k)^2}, \quad (\text{A.7})$$

where w_{ν} is a weighting factor given by $w_{\nu} = (1/\sigma_{\nu}^2)$. If the weighting factor depends on the frequency, the CMB contribution is not strictly constant in K_{CMB} units. This effect can reach up to 2 %, as the weighting factors for the *WMAP* and *Planck* maps are quite different. This is not negligible compared to the dust emission at microwave frequencies. That is the reason why we do not use inverse noise-weighting in our χ^2_{I} minimization.

In Sect. 9.2.1 we compute the frequency dependence of synchrotron emission correlated with dust. The mean spectrum of this component is given by

$$\begin{aligned} \langle \alpha_{\nu}^I(s_{353}) \rangle &= N \left\langle \sum_{k=1}^{N_{\text{pix}}} \hat{I}_{\nu}^s(k) (\hat{I}^c(k) + \hat{I}_{353}^d(k)) \right\rangle \\ &= N \left\langle \sum_{k=1}^{N_{\text{pix}}} \hat{I}_{\nu}^s(k) \hat{I}_{353}^d(k) \right\rangle, \end{aligned} \quad (\text{A.8})$$

assuming the CMB chance correlation term with synchrotron emission is zero over all the sky-patches. We detect $\langle \alpha_{\nu}^I(s_{353}) \rangle$ with high-significance in our analysis (Sect. 9.2.1), which cannot be just a chance correlation term. One would expect such a correlation, since synchrotron emission arises from the same ISM as dust emission.

Similarly for polarization, we minimize χ^2_{P} between the data and 353 GHz Stokes Q and U maps, as given by Eq. 13. The polarization CC coefficient is then given by

$$[\alpha_{\nu}^P]_{353}^{1T} = N_{\text{P}} \sum_{i=1}^2 \sum_{k=1}^{N_{\text{pix}}} [\hat{Q}_{\nu}^i(k) \cdot \hat{Q}_{353}^i(k) + \hat{U}_{\nu}^i(k) \cdot \hat{U}_{353}^i(k)], \quad (\text{A.9})$$

where N_{P} is the normalization factor for polarization. Following the same logic as described for intensity, the polarization CC coefficient at the HFI frequencies can be written as

$$\begin{aligned} [\alpha_{\nu}^P]_{353}^{1T} &= \alpha^P(c_{353}) \\ &+ N_{\text{P}} \sum_{i=1}^2 \sum_{k=1}^{N_{\text{pix}}} [\hat{Q}_{\nu}^i(k) (\hat{Q}^c(k) + \hat{Q}_{353}^d(k) + \hat{Q}_{353}^n(k))] \\ &+ N_{\text{P}} \sum_{i=1}^2 \sum_{k=1}^{N_{\text{pix}}} [\hat{U}_{\nu}^i(k) (\hat{U}^c(k) + \hat{U}_{353}^d(k) + \hat{U}_{353}^n(k))]. \end{aligned} \quad (\text{A.10})$$

Assuming the dust polarization at a given frequency is a scaled version of 353 GHz dust polarization yields $\hat{Q}_{\nu}^d(k) = \alpha_{\nu}^d \hat{Q}_{353}^d(k)$ and $\hat{U}_{\nu}^d(k) = \alpha_{\nu}^d \hat{U}_{353}^d(k)$. Putting this back into Eq. A.10 gives

$$[\alpha_{\nu}^P]_{353}^{1T} = \alpha^P(c_{353}) + \alpha^P(d_{353}). \quad (\text{A.11})$$

The polarized colour ratio does not depend on the CMB like Eq. A.5. The polarized CMB contribution $\alpha^P(c_{353})$ is strictly constant in K_{CMB} units if we do not apply any noise weighting, similar to the intensity analysis. To deal with the noise, we first smooth all the maps to 1° resolution and then perform correlation over local patches on the sky. To compute the uncertainty on the CC coefficients, we rely on Monte Carlo simulations, as discussed in Appendix B.

Appendix B: Simulations

This appendix presents the simulations of the sky emission in intensity and polarization at HFI frequencies that we use to test the CC analysis. The intensity and polarization emission components are listed in Table B.1. The simulations use a simplified model of dust emission in intensity and polarization that is good enough to provide a realistic framework to test the CC analysis. They are computed on HEALPix pixels at $N_{\text{side}} = 128$ with a 1° Gaussian beam. The Monte Carlo simulations serve two specific purposes. First, we use them to check that the CC analysis does not introduce any bias on our estimations of the mean dust spectral indices in intensity and polarization. Second, they provide realistic uncertainties on the CC coefficients, which we use in the spectral fit to separate out the dust and the CMB emission (Sect. 5.3).

B.1. Intensity

At HFI frequencies, the main diffuse emission components are the thermal dust, free-free, CMB, and CIB emission. The simulations also include instrumental noise. We now describe how we simulate each of these components.

The HI column density from the LAB survey (Kalberla et al. 2005) is taken as a proxy for thermal dust emission. We normalise the HI data to a suitable amplitude to match the observed *Planck* data at 353 GHz and extrapolate to the other HFI frequencies using an MBB spectrum with a fixed spectral index $\beta_d = 1.5$ and temperature $T_d = 18.7$ K over the whole sky. The HI data provide only a partial description of the thermal dust emission, as quoted in Planck Collaboration Int. XVII (2014). We include an additional dust component, spatially uncorrelated with the HI data, to mimic the residuals present after adopting the IR-HI correlation at 857 GHz. The additional dust-like emission is assumed to have an ℓ^{-3} power spectrum, with a normalised amplitude of $4\pi\sigma_{857}^2$ for $\ell = 2$, where σ_{857} is the residual at 857 GHz after applying the IR-HI correlation and removing the CIB contribution (Planck Collaboration Int. XVII 2014). The amplitude of the uncorrelated HI emission is normalised at 857 GHz, taken from Planck Collaboration Int. XVII (2014), and scaled to the HFI frequencies assuming $\beta_R = 2.0$ for a dust temperature of $T_R = 18.7$ K. We use the DDD H α map as a proxy for free-free emission, which we compute at HFI frequencies for a spectral index $\beta_f = -2.14$ (in K_{RJ} units) (Planck Collaboration Int. XIV 2014) and an electron temperature $T_e = 7000$ K (Dickinson et al. 2003). No dust extinction correction is applied to the DDD H α map.

For the CMB, we compute Gaussian realizations of the CMB sky from the theoretical power spectrum of the *Planck* best-fit model (Planck Collaboration XV 2014). The CIB emission is generated using the best-fit model of CIB anisotropies at 353 GHz obtained directly from the *Planck* data (Planck Collaboration XXX 2014). We assume 100% correlated CIB across all the HFI frequencies, assuming an MBB spectrum with $\beta_{\text{CIB}} = 1.3$ and $T_{\text{CIB}} = 18.4$ K. The Gaussian realizations of the instrumental noise are obtained at each frequency, using the noise variance maps (Planck Collaboration VI 2014). The noise realizations are simulated at the full resolution of the *Planck* data, before smoothing to 1° resolution and reducing the pixelization from $N_{\text{side}} = 2048$ to 128.

We compute 1000 realizations of sky maps of the additional dust component, together with the CMB and CIB anisotropies. Independent realizations of the instrumental noise are generated for each sky simulation at a given frequency. The dust com-

ponent computed from the HI map and the free-free emission traced by the H α map are kept fixed.

We analyse the 1000 simulated maps with the CC method applied to the *Planck* intensity data. We compute the mean and standard deviation of the $R_{100}^I(353, 217)$ values for each sky-patch. Both are plotted in Fig. B.1 versus the local dispersion of the 353 GHz template, σ_{353}^I . There is no bias on the estimation of the mean dust spectral index $\beta_{d,mm}^I$. We recover a mean value equal to the index of 1.5 we used for the main HI-correlated dust component. The uncertainties on $R_{100}^I(353, 217)$, and hence on $\beta_{d,mm}^I$, are associated with noise, CIB anisotropies, free-free emission, and the additional dust component. The 1σ dispersion of $\beta_{d,mm}^I$ across sky-patches for a given Monte Carlo realization is 0.03. This is smaller than the scatter of 0.07 measured for the *Planck* data. We interpret the difference as evidence for a small intrinsic dispersion in the spectral index of the dust emission.

B.2. Polarization

The simulations of the polarized sky at HFI frequencies include polarized CMB, thermal dust emission, and noise. We compute 1000 realizations of the CMB Stokes Q and U maps using the best-fit *Planck* model (Planck Collaboration XV 2014), smoothed to 1° resolution at HEALPix resolution $N_{\text{side}} = 128$. Random realizations of Gaussian noise Q and U maps are generated at each pixel using the 3×3 noise covariance matrix defined at $N_{\text{side}} = 2048$. The noise maps are then smoothed to 1° resolution and projected on to a HEALPix map at $N_{\text{side}} = 128$. We generate independent realizations of the instrumental noise to mimic the detector sets at 353 GHz (Sect. 2.1.2).

For polarized thermal dust emission, we use the following model:

$$[Q_v^d, U_v^d] = p_d \left(\frac{\nu}{353 \text{ GHz}} \right)^{\beta_{d,mm}^d} \frac{B_\nu(T_d)}{B_{353}(T_d)} I_{353}^d [\cos 2\psi_d, \sin 2\psi_d]. \quad (\text{B.1})$$

Here p_d , I_{353}^d , and ψ_d are the polarization fraction, the dust intensity at 353 GHz, and the polarization angle, respectively. We fix p_d to a constant value of 10% over the whole sky. The I_{353}^d map is that obtained by Planck Collaboration XI (2014) from the spectral fit to the high frequency *Planck* and IRAS 100 μm data, with an MBB model. For the dust polarization, we use an MBB spectrum with $\beta_{d,mm}^d = 1.7$ and $T_d = 18.7$ K, constant over the whole sky. We derive ψ_d from the 1° smoothed *Planck* Stokes maps using the relation

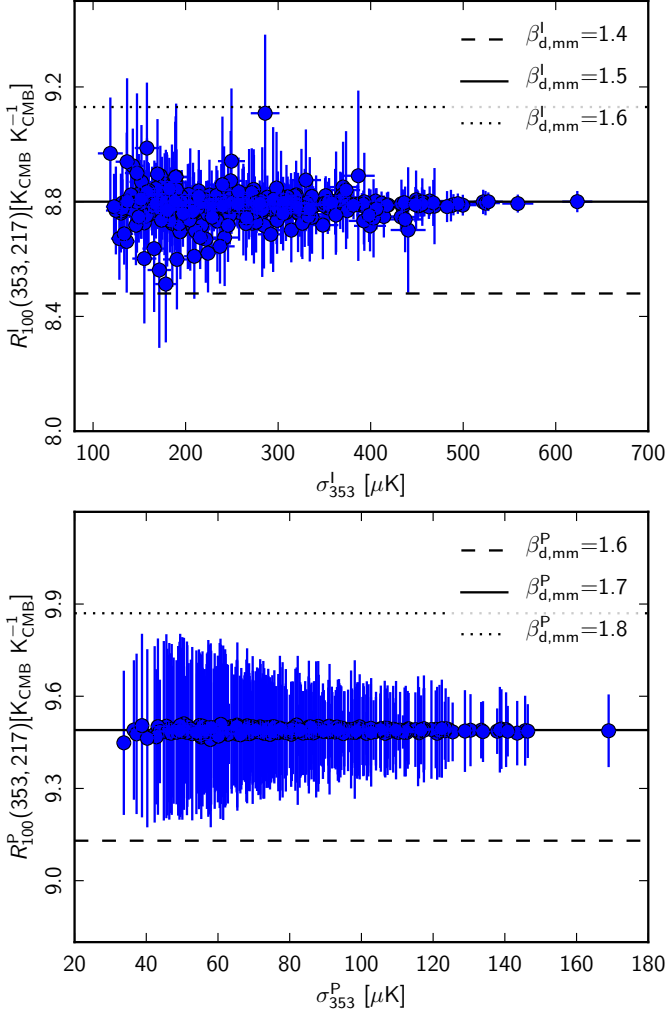
$$\psi_d(k) = -\frac{1}{2} \tan^{-1} \left[\frac{U_{\nu_2}^{\text{obs}}(k) - U_{\nu_1}^{\text{obs}}(k)}{Q_{\nu_2}^{\text{obs}}(k) - Q_{\nu_1}^{\text{obs}}(k)} \right]. \quad (\text{B.2})$$

We choose ν_1 and ν_2 as the 143 and 353 GHz, respectively. The difference between the two frequencies removes the CMB contribution.

We analyse 1000 polarized simulated maps using the CC analysis as applied to the *Planck* data. We compute the mean and the standard deviation of the $R_{100}^P(353, 217)$ for each sky-patch. The plot of $R_{100}^P(353, 217)$ versus σ_{353}^P is shown in Fig. B.1. We find no bias in the estimation of $R_{100}^P(353, 217)$ and hence in the measurement of $\beta_{d,mm}^P$. The 1σ dispersion of $\beta_{d,mm}^P$ across sky-patches for a given simulation is 0.07. The 1σ dispersion of $\beta_{d,mm}^P$ from the simulations is small compared to that measured from the *Planck* data, this is because we do not take into account systematic effects in the simulations.

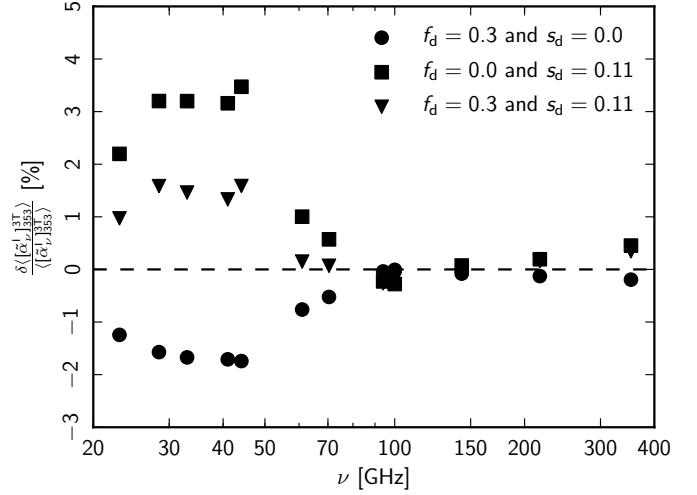
Table B.1. The ancillary data sets and models used in the Monte Carlo simulations.

Components	Tracer	Model	Parameters	References
CMB	TT spectrum		<i>Planck</i> best-fit parameters	Planck Collaboration XV (2014)
Thermal dust	HI template	MBB	$(\beta_d, T_d) = (1.5, 18.7 \text{ K})$	Planck Collaboration Int. XVII (2014)
IR-HI excess	Residual at 857 GHz	MBB	$(\beta_R, T_R) = (2.0, 18.7 \text{ K})$	Planck Collaboration Int. XVII (2014)
Free-free	H α map	PL	$(\beta_f, T_e) = (-2.14, 7000 \text{ K})$	Dickinson et al. (2003)
CIB	CIB spectrum	MBB	$(\beta_{\text{CIB}}, T_{\text{CIB}}) = (1.3, 18.4 \text{ K})$	Planck Collaboration XXX (2014)
Statistical noise	Variance maps		(II, IQ, IU, QQ, QU, UU)	Planck Collaboration VI (2014)
Polarized thermal dust	Model	MBB	$(\beta_d, T_d) = (1.7, 18.7 \text{ K})$	

**Fig. B.1.** $R_{100}(353, 217)$ colour ratios from the Monte Carlo simulations for intensity (*top*) and polarization (*bottom*). The two plots show that the CC analysis does not introduce any bias on the estimation of $\beta_{d,mm}$.

Appendix C: Mean dust SED with dust extinction and scattering correction on the H α template

The mean dust SED for intensity presented in this paper is obtained using the three-template fit with no extinction and dust scattering correction from the DDD H α template. The effect of dust extinction (f_d) on the H α template is described in equation 3 of [Dickinson et al. \(2003\)](#), whereas the effect of dust scattering (s_d) on the H α template is described in equation 26 of [Bennett et al. \(2013\)](#). The mean measured value of s_d is 0.11

**Fig. C.1.** Fractional change in the mean dust SED with respect to the reference dust SED presented in this paper, for different combinations of f_d and s_d corrections on the DDD H α template.

R (MJy sr^{-1}) $^{-1}$ in high Galactic latitude regions ([Lehtinen et al. 2010](#); [Witt et al. 2010](#); [Seon & Witt 2012](#); [Brandt & Draine 2012](#); [Bennett et al. 2013](#)). To check the impact of the f_d and s_d corrected H α template on the mean dust SED, we repeat the analysis with different combinations of f_d and s_d . The three different combinations of f_d and s_d corrected H α templates we choose are: $f_d = 0.3$ and $s_d = 0.0$ R (MJy sr^{-1}) $^{-1}$; $f_d = 0.0$ and $s_d = 0.11$ R (MJy sr^{-1}) $^{-1}$; and $f_d = 0.3$ and $s_d = 0.11$ R (MJy sr^{-1}) $^{-1}$. The fractional change in the mean dust SED with respect to the reference dust SED ($f_d = 0.0$ and $s_d = 0.0$ R (MJy sr^{-1}) $^{-1}$) is presented in Fig. C.1. At higher frequencies ($\nu \geq 100$ GHz), the impact of both dust extinction and scattering is negligible. However at frequencies $\nu \leq 50$ GHz, the fractional change on the mean SED can go as high as $\pm 4\%$. The f_d and s_d parameters are degenerate, although their effect on the derived best-fit parameter of models DI+AI, DII+AI, and DII+AII, listed in Table 4, is very small.

Appendix D: Power spectra of the templates

In this section, we compute the temperature power spectra of the three templates at 1° resolution: 408 MHz; DDD H α ; and 353 GHz dust template. The *Planck* 353 GHz map contains a significant component of CMB anisotropies. Taking the SMICA map ([Planck Collaboration XII 2014](#)) as a proxy for the CMB map, we remove its contribution from the 353 GHz total map. These spectra are combined with the SEDs from this paper to compute the contributions of each emission component to the mi-

crowwave sky emission as a function of angular scales in [Planck Collaboration I \(2014\)](#) (see their Figs. 27 and 28).

For the computation of the power spectra, we consider the four diffuse Galactic masks based on the percentage of the sky retained (f_{sky}), i.e., G40, G60, G70 and G80 ([Planck Collaboration XV 2014](#)). The same set of masks have been used in the likelihood analysis of the 2013 *Planck* data release ([Planck Collaboration XV 2014](#)). The power spectra are computed only at low multipoles ($\ell < 100$) with *PolSpice* v2.9.0 ([Chon et al. 2004](#)), corrected for the masking, beam, and pixel window effect. Figure D.1 presents binned power spectra of the three templates: 408 MHz, DDD $\text{H}\alpha$, and SMICA-subtracted 353 GHz maps as a function of the Galactic masks. The uncertainties on the binned power spectra include only the statistical variance and not the cosmic variance.

At low multipoles, $\ell < 100$, the three power spectra are well-fit with a power-law model. Using this assumption, the measured power spectra are written as $C_\ell = A \times (\ell/100)^\alpha$. Here A represents the normalized amplitude at $\ell = 100$ and α represents the slope of the power-law for a given template. We fix α based on the measured spectra and only fit for the amplitudes as a function of the Galactic masks. We find that the slope of the 408 MHz spectra over all the Galactic masks is consistent with -2.5 . In case of DDD $\text{H}\alpha$ template is -2.2 over the masks and the same for the SMICA-subtracted 353 GHz template is -2.4 . The results of the power-law fit for the three templates and different Galactic masks are shown as a dashed lines in Fig. D.1. The amplitudes of each of the templates as a function of the Galactic masks (or f_{sky}) are listed in Table D.1.

The amplitudes of the given templates vary nonlinearly as a function of f_{sky} . They can be fitted with a second-order polynomial in a $\log A - \log f_{\text{sky}}$ plane. Combining the ν , ℓ , and f_{sky} dependence, we analytically model the power spectra of the diffuse synchrotron, free-free, and dust emission components for intensity. For amplitude normalization, we made an assumption on the nature of the synchrotron and free-free emission. We assume a single power-law model for the synchrotron emission from 408 MHz to microwave frequencies, $\nu \leq 353$ GHz. For free-free emission, we assume a single power-law model at microwave frequencies, with a mean electron temperature of 7000 K ([Dickinson et al. 2003](#)). The power spectra of the three diffuse emission components, in $\mu\text{K}_{\text{RJ}}^2$ units, are

$$C_\ell^f = 0.068 \times \left(\frac{f_{\text{sky}}}{0.6}\right)^{[6.17 + 3.60 \ln(f_{\text{sky}}/0.6)]} \times \left(\frac{\ell}{100}\right)^{-2.2} \times \left(\frac{\nu}{23 \text{ GHz}}\right)^{-4.28}, \quad (\text{D.1})$$

$$C_\ell^s = 2.8 \times 10^9 \times \left(\frac{f_{\text{sky}}}{0.6}\right)^{[2.03 + 3.57 \ln(f_{\text{sky}}/0.6)]} \times \left(\frac{\ell}{100}\right)^{-2.5} \times \left(\frac{\nu}{0.408 \text{ GHz}}\right)^{-6.0}, \quad (\text{D.2})$$

$$C_\ell^d = 13.60 \times \left(\frac{f_{\text{sky}}}{0.6}\right)^{[4.69 + 6.85 \ln(f_{\text{sky}}/0.6)]} \times \left(\frac{\ell}{100}\right)^{-2.4} \times \mathcal{D}_\nu, \quad (\text{D.3})$$

where \mathcal{D}_ν is a spectral model of the dust emission given by one of the three models presented in Eqs. 25, 26, and 27. The derived analytical model of these power spectra are valid in the frequency range 20 to 353 GHz, and for f_{sky} between 0.4 and 0.8.

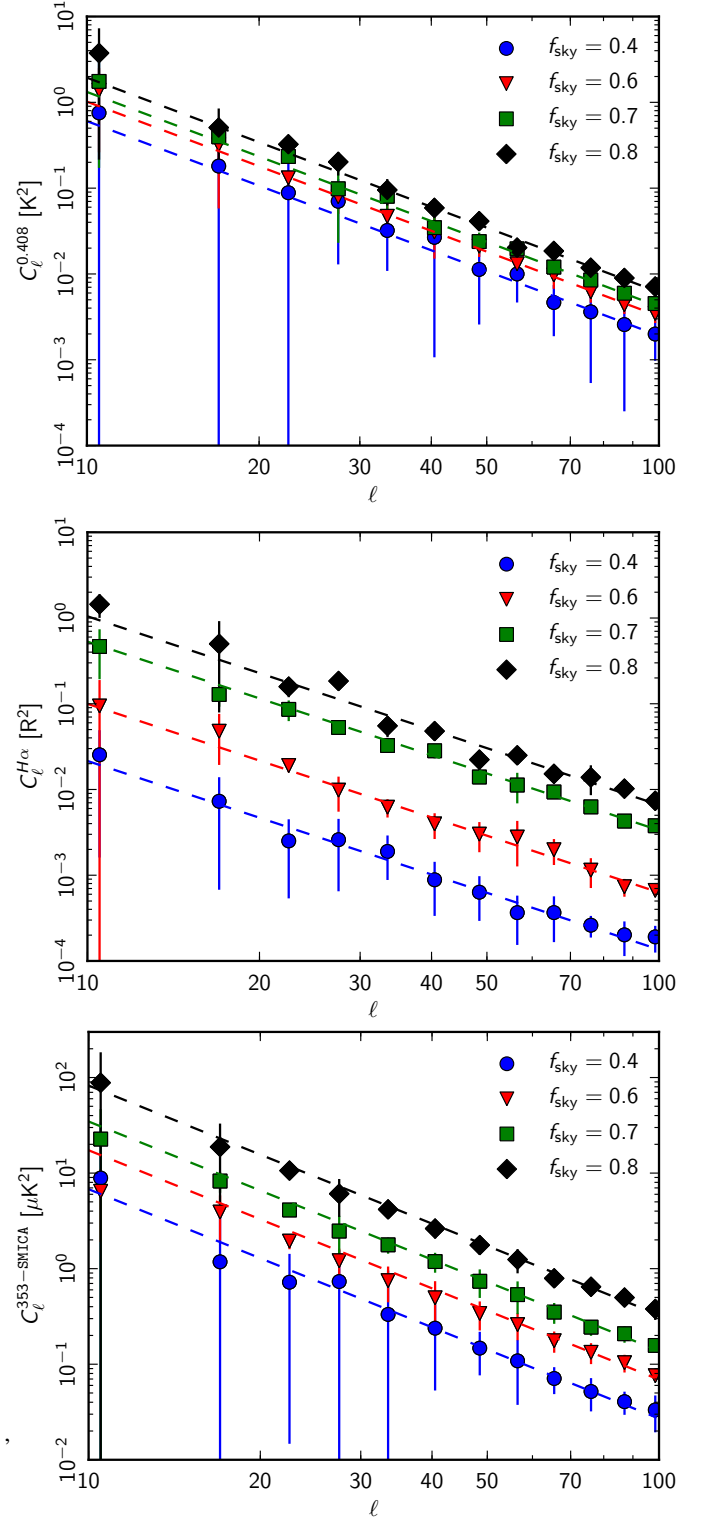


Fig. D.1. Power spectra of the 408 MHz, DDD $\text{H}\alpha$, and SMICA-subtracted 353 GHz templates, smoothed to 1° resolution for different Galactic masks (or f_{sky}).

13, France

² African Institute for Mathematical Sciences, 6-8 Melrose Road, Muizenberg, Cape Town, South Africa

³ Agenzia Spaziale Italiana Science Data Center, Via del Politecnico snc, 00133, Roma, Italy

⁴ Agenzia Spaziale Italiana, Viale Liegi 26, Roma, Italy

⁵ Astrophysics Group, Cavendish Laboratory, University of Cambridge, J J Thomson Avenue, Cambridge CB3 0HE, U.K.

⁶ Astrophysics & Cosmology Research Unit, School of Mathematics, Statistics & Computer Science, University of KwaZulu-Natal,

¹ APC, AstroParticule et Cosmologie, Université Paris Diderot, CNRS/IN2P3, CEA/Irfu, Observatoire de Paris, Sorbonne Paris Cité, 10, rue Alice Domon et Léonie Duquet, 75205 Paris Cedex

Table D.1. Amplitudes of the power spectra, normalized at $\ell = 100$, as a function of f_{sky} .

Gal. masks	f_{sky}	Amplitudes		
		$A_{0.408}$ [10^{-3} K^2] ($\alpha = -2.5$)	$A_{\text{H}\alpha}$ [10^{-3} R^2] ($\alpha = -2.2$)	$A_{353\text{--SMICA}}$ [μK^2] ($\alpha = -2.4$)
G40	0.40	1.91 ± 0.49	0.136 ± 0.024	0.027 ± 0.004
G60	0.60	3.22 ± 0.31	0.630 ± 0.037	0.069 ± 0.006
G70	0.70	4.18 ± 0.38	3.346 ± 0.197	0.138 ± 0.011
G80	0.80	6.13 ± 0.49	6.605 ± 0.321	0.328 ± 0.020

Westville Campus, Private Bag X54001, Durban 4000, South Africa

⁷ Atacama Large Millimeter/submillimeter Array, ALMA Santiago Central Offices, Alonso de Cordova 3107, Vitacura, Casilla 763 0355, Santiago, Chile

⁸ CITA, University of Toronto, 60 St. George St., Toronto, ON M5S 3H8, Canada

⁹ CNR - ISTI, Area della Ricerca, via G. Moruzzi 1, Pisa, Italy

¹⁰ CNRS, IRAP, 9 Av. colonel Roche, BP 44346, F-31028 Toulouse cedex 4, France

¹¹ California Institute of Technology, Pasadena, California, U.S.A.

¹² Centro de Estudios de Física del Cosmos de Aragón (CEFCA), Plaza San Juan, 1, planta 2, E-44001, Teruel, Spain

¹³ Computational Cosmology Center, Lawrence Berkeley National Laboratory, Berkeley, California, U.S.A.

¹⁴ DSM/Irfu/SPP, CEA-Saclay, F-91191 Gif-sur-Yvette Cedex, France

¹⁵ DTU Space, National Space Institute, Technical University of Denmark, Elektrovej 327, DK-2800 Kgs. Lyngby, Denmark

¹⁶ Département de Physique Théorique, Université de Genève, 24, Quai E. Ansermet, 1211 Genève 4, Switzerland

¹⁷ Departamento de Física Fundamental, Facultad de Ciencias, Universidad de Salamanca, 37008 Salamanca, Spain

¹⁸ Departamento de Física, Universidad de Oviedo, Avda. Calvo Sotelo s/n, Oviedo, Spain

¹⁹ Department of Astronomy and Astrophysics, University of Toronto, 50 Saint George Street, Toronto, Ontario, Canada

²⁰ Department of Astrophysics/IMAPP, Radboud University Nijmegen, P.O. Box 9010, 6500 GL Nijmegen, The Netherlands

²¹ Department of Physics & Astronomy, University of British Columbia, 6224 Agricultural Road, Vancouver, British Columbia, Canada

²² Department of Physics and Astronomy, Dana and David Dornsife College of Letter, Arts and Sciences, University of Southern

California, Los Angeles, CA 90089, U.S.A.

²³ Department of Physics and Astronomy, University College London, London WC1E 6BT, U.K.

²⁴ Department of Physics, Gustaf Hållströmin katu 2a, University of Helsinki, Helsinki, Finland

²⁵ Department of Physics, Princeton University, Princeton, New Jersey, U.S.A.

²⁶ Department of Physics, University of California, Santa Barbara, California, U.S.A.

²⁷ Department of Physics, University of Illinois at Urbana-Champaign, 1110 West Green Street, Urbana, Illinois, U.S.A.

²⁸ Dipartimento di Fisica e Astronomia G. Galilei, Università degli Studi di Padova, via Marzolo 8, 35131 Padova, Italy

²⁹ Dipartimento di Fisica e Scienze della Terra, Università di Ferrara, Via Saragat 1, 44122 Ferrara, Italy

³⁰ Dipartimento di Fisica, Università La Sapienza, P. le A. Moro 2, Roma, Italy

³¹ Dipartimento di Fisica, Università degli Studi di Milano, Via Celoria, 16, Milano, Italy

³² Dipartimento di Fisica, Università degli Studi di Trieste, via A. Valerio 2, Trieste, Italy

³³ Dipartimento di Fisica, Università di Roma Tor Vergata, Via della Ricerca Scientifica, 1, Roma, Italy

³⁴ Discovery Center, Niels Bohr Institute, Blegdamsvej 17, Copenhagen, Denmark

³⁵ Dpto. Astrofísica, Universidad de La Laguna (ULL), E-38206 La Laguna, Tenerife, Spain

³⁶ European Southern Observatory, ESO Vitacura, Alonso de Cordova 3107, Vitacura, Casilla 19001, Santiago, Chile

³⁷ European Space Agency, ESAC, Planck Science Office, Camino bajo del Castillo, s/n, Urbanización Villafranca del Castillo,

- Villanueva de la Cañada, Madrid, Spain
- ³⁸ European Space Agency, ESTEC, Keplerlaan 1, 2201 AZ Noordwijk, The Netherlands
- ³⁹ Helsinki Institute of Physics, Gustaf Hållströmin katu 2, University of Helsinki, Helsinki, Finland
- ⁴⁰ INAF - Osservatorio Astronomico di Padova, Vicolo dell'Osservatorio 5, Padova, Italy
- ⁴¹ INAF - Osservatorio Astronomico di Roma, via di Frascati 33, Monte Porzio Catone, Italy
- ⁴² INAF - Osservatorio Astronomico di Trieste, Via G.B. Tiepolo 11, Trieste, Italy
- ⁴³ INAF/IASF Bologna, Via Gobetti 101, Bologna, Italy
- ⁴⁴ INAF/IASF Milano, Via E. Bassini 15, Milano, Italy
- ⁴⁵ INFN, Sezione di Bologna, Via Imerio 46, I-40126, Bologna, Italy
- ⁴⁶ INFN, Sezione di Roma 1, Università di Roma Sapienza, Piazzale Aldo Moro 2, 00185, Roma, Italy
- ⁴⁷ INFN/National Institute for Nuclear Physics, Via Valerio 2, I-34127 Trieste, Italy
- ⁴⁸ IPAG: Institut de Planétologie et d'Astrophysique de Grenoble, Université Joseph Fourier, Grenoble 1 / CNRS-INSU, UMR 5274, Grenoble, F-38041, France
- ⁴⁹ Imperial College London, Astrophysics group, Blackett Laboratory, Prince Consort Road, London, SW7 2AZ, U.K.
- ⁵⁰ Infrared Processing and Analysis Center, California Institute of Technology, Pasadena, CA 91125, U.S.A.
- ⁵¹ Institut d'Astrophysique Spatiale, CNRS (UMR8617) Université Paris-Sud 11, Bâtiment 121, Orsay, France
- ⁵² Institut d'Astrophysique de Paris, CNRS (UMR7095), 98 bis Boulevard Arago, F-75014, Paris, France
- ⁵³ Institute for Space Sciences, Bucharest-Magurale, Romania
- ⁵⁴ Institute of Astronomy, University of Cambridge, Madingley Road, Cambridge CB3 0HA, U.K.
- ⁵⁵ Institute of Theoretical Astrophysics, University of Oslo, Blindern, Oslo, Norway
- ⁵⁶ Instituto de Astrofísica de Canarias, C/Vía Láctea s/n, La Laguna, Tenerife, Spain
- ⁵⁷ Instituto de Astronomia, Geofísica e Ciências Atmosféricas, Universidade de São Paulo, São Paulo, SP 05508-090, Brazil
- ⁵⁸ Instituto de Física de Cantabria (CSIC-Universidad de Cantabria), Avda. de los Castros s/n, Santander, Spain
- ⁵⁹ Jet Propulsion Laboratory, California Institute of Technology, 4800 Oak Grove Drive, Pasadena, California, U.S.A.
- ⁶⁰ Jodrell Bank Centre for Astrophysics, Alan Turing Building, School of Physics and Astronomy, The University of Manchester, Oxford Road, Manchester, M13 9PL, U.K.
- ⁶¹ Kavli Institute for Cosmology Cambridge, Madingley Road, Cambridge, CB3 0HA, U.K.
- ⁶² LAL, Université Paris-Sud, CNRS/IN2P3, Orsay, France
- ⁶³ LERMA, CNRS, Observatoire de Paris, 61 Avenue de l'Observatoire, Paris, France
- ⁶⁴ Laboratoire AIM, IRFU/Service d'Astrophysique - CEA/DSM - CNRS - Université Paris Diderot, Bât. 709, CEA-Saclay, F-91191 Gif-sur-Yvette Cedex, France
- ⁶⁵ Laboratoire Traitement et Communication de l'Information, CNRS (UMR 5141) and Télécom ParisTech, 46 rue Barrault F-75634 Paris Cedex 13, France
- ⁶⁶ Laboratoire de Physique Subatomique et de Cosmologie, Université Joseph Fourier Grenoble I, CNRS/IN2P3, Institut National Polytechnique de Grenoble, 53 rue des Martyrs, 38026 Grenoble cedex, France
- ⁶⁷ Laboratoire de Physique Théorique, Université Paris-Sud 11 & CNRS, Bâtiment 210, 91405 Orsay, France
- ⁶⁸ Lawrence Berkeley National Laboratory, Berkeley, California, U.S.A.
- ⁶⁹ Max-Planck-Institut für Astrophysik, Karl-Schwarzschild-Str. 1, 85741 Garching, Germany
- ⁷⁰ National University of Ireland, Department of Experimental Physics, Maynooth, Co. Kildare, Ireland
- ⁷¹ Niels Bohr Institute, Blegdamsvej 17, Copenhagen, Denmark
- ⁷² Observational Cosmology, Mail Stop 367-17, California Institute of Technology, Pasadena, CA, 91125, U.S.A.
- ⁷³ Optical Science Laboratory, University College London, Gower Street, London, U.K.
- ⁷⁴ SISSA, Astrophysics Sector, via Bonomea 265, 34136, Trieste, Italy
- ⁷⁵ School of Physics and Astronomy, Cardiff University, Queens Buildings, The Parade, Cardiff, CF24 3AA, U.K.
- ⁷⁶ Space Sciences Laboratory, University of California, Berkeley, California, U.S.A.
- ⁷⁷ Special Astrophysical Observatory, Russian Academy of Sciences, Nizhnij Arkhyz, Zelenchukskiy region, Karachai-Cherkessian Republic, 369167, Russia
- ⁷⁸ Sub-Department of Astrophysics, University of Oxford, Keble Road, Oxford OX1 3RH, U.K.
- ⁷⁹ UPMC Univ Paris 06, UMR7095, 98 bis Boulevard Arago, F-75014, Paris, France
- ⁸⁰ Université de Toulouse, UPS-OMP, IRAP, F-31028 Toulouse cedex 4, France
- ⁸¹ Universities Space Research Association, Stratospheric Observatory for Infrared Astronomy, MS 232-11, Moffett Field, CA 94035,

U.S.A.

⁸² University of Granada, Departamento de Física Teórica y del Cosmos, Facultad de Ciencias, Granada, Spain

⁸³ University of Granada, Instituto Carlos I de Física Teórica y Computacional, Granada, Spain

⁸⁴ Warsaw University Observatory, Aleje Ujazdowskie 4, 00-478 Warszawa, Poland